Impact of the Cu Current Collector Grade and Ink Solid Fraction on the Electrochemical Performance of Silicon-Based Electrodes for Li-Ion Batteries

Lucas Huet, Hippolyte Houisse, Natalie Herkendaal, Thomas Devic, Lionel Roué, Bernard Lestriez

Impact of the Cu Current Collector Grade and Ink Solid Fraction on the Electrochemical Performance of Silicon-Based Electrodes for Li-Ion Batteries

*Lucas Huet, Hippolyte Houisse, Natalie Herkendaal, Thomas Devic, Lionel Roué, and Bernard Lestriez**

Lucas Huet, Hippolyte Houisse, Natalie Herkendaal, Thomas Devic, Bernard Lestriez
Nantes Université, CNRS, Institut des Matériaux de Nantes Jean Rouxel, IMN, Nantes F-44000, France
E-mail: Bernard.Lestriez@cnrs-imn.fr

Lucas Huet, Hippolyte Houisse, Natalie Herkendaal, Lionel Roué
Centre Énergie, Matériaux, Télécommunications (EMT), Institut National de la Recherche Scientifique (INRS), Varennes, Quebec J3X 1S2, Canada

Keywords: Silicon anode, Carboxymethyl cellulose binder, Current collector, Solid fraction, Solid loading, Coordination bond, Li-ion batteries

Abstract

The influence of the Cu current collector grade (cold-rolled, annealed, or textured) and the ink solid fraction (SF) on the performance of Si-based electrodes for Li-ion batteries is investigated. Two binders are considered for this study: one of carboxymethylcellulose and citric acid, and the other which consists of the same organic components with added Zn(II) cations. These ones crosslink the carboxylate moieties through coordination bonds. The fracture behavior and cyclability of the Zn-free electrodes show a strong dependence on the Cu current collector grade. For this formulation, which has lower cohesion, the increase in electrode adhesion from the roughening of the surface of the current collector and/or the decrease of the current collector yield strength contribute to mitigate the electrode mechanical damage, therefore improving its cyclability. Such a dependence is not observed for the Zn cross-linked electrodes which have a higher cohesion. Regarding the impact of the ink solid fraction, when a higher SF is used, the capacity retention and coulombic efficiency are enhanced for both formulations, though much more significantly for the Zn-free formulation. The underlying mechanism causing this improvement may be partially related to the enhanced adsorption of binder on silicon particles with increasing SF.

1. Introduction

Silicon is a promising negative electrode material for next generation Li-ion batteries due to its high theoretical gravimetric and volumetric capacities. At the highest lithiation stoichiometry, *i.e.* $Li_{15}Si_4$, its capacity reaches ~3600 $mAh.g^{-1}$ and ~2200 $mAh.cm^{-3}$, respectively. However, its well-known limitations, which are mainly related to its high volumetric variation (up to 280% at full lithiation), are not yet fully resolved.[1] One of these is electrode cracking and delamination which is known to be detrimental to electrochemical performance. To circumvent these mechanical issues, various electrode formulations have been investigated, particularly in regards to the nature of the binder, as it plays a key role on the electrode mechanical behavior.[2,3] Other electrode components, such as the Cu current collector, but also some electrode processing parameters such as the ink solid fraction (SF), are also likely to impact on the mechanical and electrochemical properties of Si-based electrodes.

There are many metallurgical grades of copper foil with different mechanical properties depending on their respective manufacturing processes. These properties, namely elastic modulus and yield strength, can dramatically impact the fracture mechanics of a thin film covering the current collector,[4–6] as is the case of electrode film. Though works have shown in the past that modifying the surface of the current collector can influence the cyclability of silicon-based electrodes,[7–11] to our knowledge, the influence of the copper current collector metallurgical grade has never been investigated for electrodes containing alloying materials with high volume variation like silicon.

Second, the influence of the SF, which is the dry matter fraction of the ink formulation, has already been studied but only for positive electrode formulations.[12–14] Even though the number of studies available is small, they all yield very interesting results. In fact, there is an optimal solid fraction for which the composite electrode elements (active material, conductive additive, and binder) are most homogeneously dispersed. Below this optimum value, the amount of solvent in the ink is too high and particle sedimentation and/or binder migration occur during drying, which results in phase segregation across the electrode film.[12,13] Above this optimum value, the ink viscosity is too high, which hinders the de-agglomeration of the electrode components and their efficient dispersion in the ink, again resulting in phase segregation.[12] In both cases, the electrochemical performance is reduced. Further, solid fraction tuning improves electrode characteristics such as adhesion and conductivity (among others) as Das et al. have shown for $LiFePO_4$ electrodes.[14]

As such, in the present study, the influence of the Cu current collector (Cu CC) grade and the ink SF on the performance of Si-based electrodes is investigated. Two pre-optimized

binders were considered for this study: a purely organic binder of carboxymethylcellulose and citric acid, which has been used as a reference in previous works,[15–17] and the other which consists of the same organic components together with a divalent cation (here Zn(II)) which has been shown to further crosslink the carboxylate moieties through coordination bonds, enhancing the mechanical properties and acting to some extent as an artificial SEI in the resulting electrodes.[15–17] Here, we show that the Cu CC grade and the SF significantly influence the cyclability of silicon-based electrodes while highlighting the robustness of the formulation including cross-linked polymers with Zn(II) cations whose electrochemical behavior appears much less sensitive to the Cu CC grade and ink SF.

2. Results and discussion

Inks for electrode fabrication were prepared by mixing a fixed amount of silicon and conducting additive (graphene) with a varying amount of binder solution whose concentration was tuned to systematically reach a final Si/graphene/binder composition of approximately 70:10:20 $_w$%. The reference binder solution consists of sodium carboxymethylcellulose (NaCMC) dissolved in a buffer solution of citric acid (CA) and sodium or potassium hydroxide. Then, Zn(II) ion are introduced in the form of a salt ($ZnSO_4$, $Zn(NO_3)_2$) or an oxide (ZnO) for coordinated formulations. The effects of the nature of the metallic precursor[17] and the coordination ratio,[16] which is the molar ratio of Zn over COOH moieties, have been previously evaluated. Interestingly, regardless of the Zn(II) ion source, the electrochemical performance is significantly improved by the formation of a cross-linked network of Zn-carboxylate coordination bonds as compared to the reference (Zn-free) binder electrodes. The Zn cross-linked binder particularly improves the electrode mechanical properties[17] and solid electrolyte interphase (SEI) stability,[15] thus improving the overall electrochemical performance. **Table 1** and Table S1 summarize the $ZnSO_4$ and Zn-free formulations which are used in this study. Their areal mass loading was fixed at 1.75 ± 0.1 $mg_{Si}.cm^{-2}$. The electrodes were not calendered and their porosity at the pristine state was estimated at around 60%.

Table 1. Composition of the electrode for the $ZnSO_4$ and reference (Zn-free) formulations.

Formulation name		**Electrode composition [$_w$%]**					
Salt	*Coord. ratio*	*Silicon*	*Graphene*	*NaCMC*	*Citric acid*	*NaOH*	*Zn precursor*
Zn-free	0	73.6	11	7.2	7.4	0.8	0
$ZnSO_4$	0.22	70.1	10.5	6.8	7	0.7	4.9

2.1. Cu current collector mechanical properties and their influence on electrochemical performance

Figures 1a to 1d show the evolution over cycling of the specific discharge capacities and coulombic efficiencies (CE) of the reference (21.4% SF) and the $ZnSO_4$ (22.3% SF) electrodes (averaged over 3 to 8 cells) made with either a cold rolled (C.-R.), annealed (Ann.), or textured (Txt.) Cu CCs. The charge capacity is not discussed/shown as we expect its trends to be similar to the discharge capacity ones. When the Ann. or Txt. Cu CCs are used, the capacity retention is significantly enhanced as compared to the C.-R. Cu CC for the Zn-free formulation. Their 60^{th} cycle capacities are approximately 2230, 1930, and 1740 $mAh.g_{Si}^{-1}$ for the Ann., Txt., and C.-R. Cu CC, respectively. The coulombic efficiency (CE) is also affected by the nature of the current collector for electrodes of this same formulation. The 1^{st} cycle CE are 82.8, 84.9, and 81.1% for the Ann., Txt., and C.-R. Cu CCs, respectively, and the CE plateau is at around 99.5% for the Ann. Cu CC and 99.4% for the C.R. Cu CC from the 20^{th} cycle. The average CE from the 20^{th} to 65^{th} cycle was not obtained for the Txt. Cu CC because the CE was over 100% for most of the cycles, purportedly due to parasitic reactions at the Li counter-electrode during the charge. In contrast, for the formulation containing $ZnSO_4$, the impact of the Cu CC's nature is very limited as shown by the 60^{th} cycle capacities which are 2550, 2320, and 2520 $mAh.g_{Si}^{-1}$ for the Ann., Txt., and C.-R. Cu CCs, respectively. The 1^{st} cycle CE are 86.2, 85.5, and 84.5% for the Ann., Txt. and C.-R. Cu CCs, respectively. These stabilize at around 99.4, 99.5, and 99.2% from the 20^{th} cycle on for the Ann., Txt., and C.-R. Cu CCs, respectively. Complementary information on electrochemical performance is gathered in Table S2 for each formulation tested in this study. In summary, it clearly appears that the Ann. and Txt. Cu CCs improve the capacity retention over the C.-R. Cu CC for the Zn-free formulation, which is not the case for the $ZnSO_4$ formulation. These results also show that regardless of the Cu CC grade, the cyclability and the 1^{st} cycle CE are increased by the crosslinking of the binder with Zn. The latter formulation has better mechanical properties than the former, *i.e.* superior cohesion, hardness, and elastic modulus, which ultimately lead to a reduced expansion of the electrode during electrochemical cycling.[17]

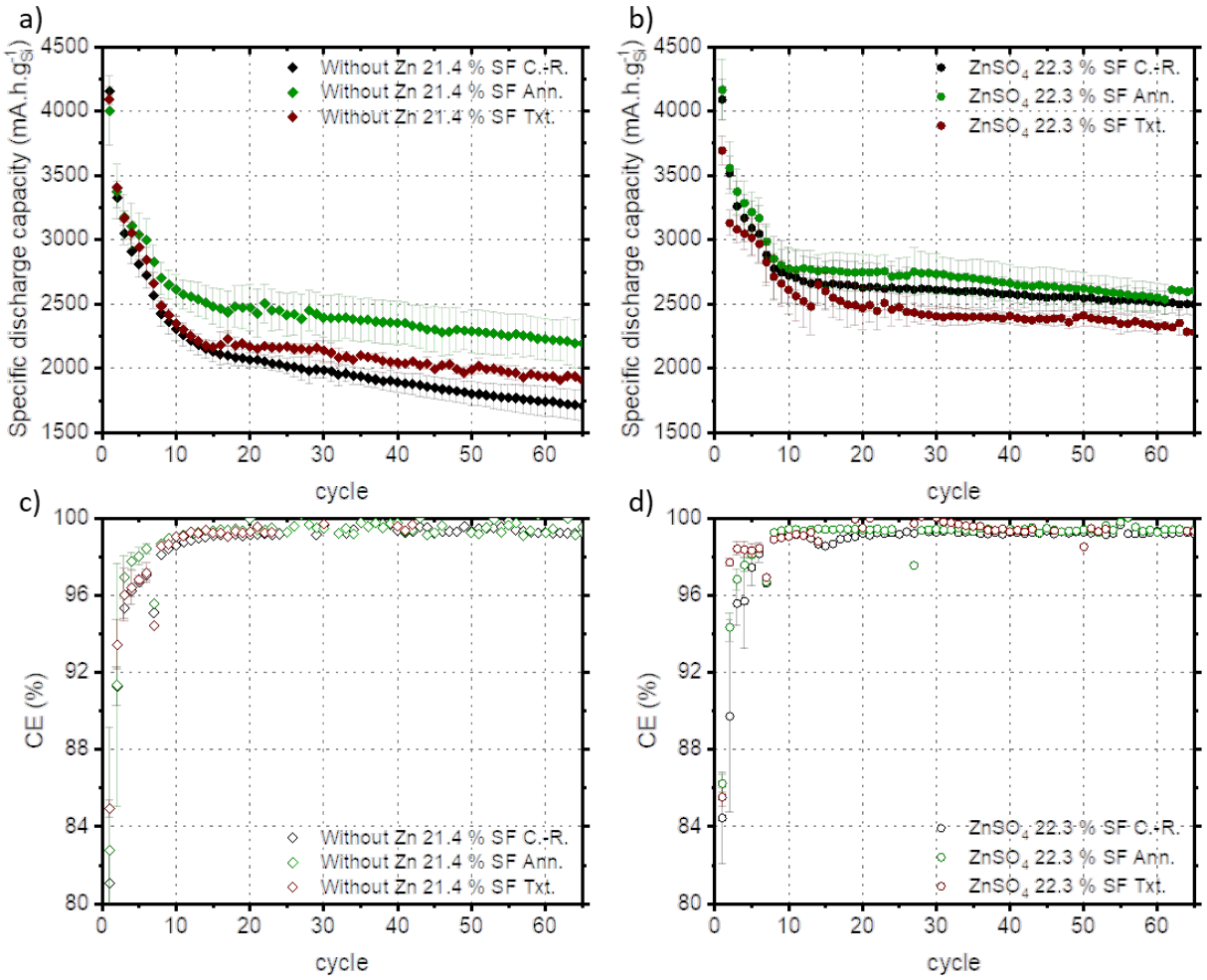

Figure 1. Mean specific discharge capacity and CE as a function of cycle number of electrodes with either cold rolled, annealed, or textured Cu current collector: (a, b) Zn-free formulation; (c, d) $ZnSO_4$ formulation. The electrodes were cycled at C/40 for the 1st cycle, then C/20 for 5 cycles, and C/10 for the remaining cycles. Their active mass loading was 1.75 ± 0.1 $mg_{Si}.cm^{-2}$. The mean and standard deviation values were determined using a minimum of 3 electrodes for each formulation.

In parallel, the cracking patterns of Zn-free and ZnSO4 electrodes on the different Cu CC were observed after 1 cycle with a scanning electron microscope (SEM) as shown in Figure 2. The study of cracking after the first cycle is relevant since the operando optical microscopy analysis did not reveal any further crack formation or propagation after the subsequent few cycles (see Video S1 and S2 and Figure S1). This is also in accordance with our previous operando optical microscopy observations on Si-based electrodes, showing that the larger cracks form during the first delithiation and then close and open at the same places in the electrode film upon successive lithiation/delithiation cycles.[18] This means that most of the

electrode mechanical degradation in the form of large cracks happens during the first cycle. This is expected since the lithiation and delithiation reach their maximum during the 1st cycle, so does the corresponding strain, and therefore the induced stress. Nonetheless, additional mechanical damage may be anticipated after repeated cycling because of material fatigue[19] and the accumulation of SEI products in the pores and cracks of the electrode,[20] reducing the free space for electrode expansion. This additional damage may be the cause of the more gradual decrease in capacity observed after the first cycle. The latter can also have as a complementary origin the growth of the SEI electrically insulating the active material.[21]

The crack pattern on each electrode resembles that of mud cracking. The cracks run in different directions, merging into a network and in doing so, form islands of electrode coating. Even if it is not as obvious in the Zn-free electrode with a C.-R. Cu CC, cracks running in various directions can be seen. Such seemingly random crack orientation indicates that the stress which generates them is multiaxial.[4,22] Interestingly, the formation of such cracks in coatings, (thin) films, and layered material happens when they are under tension.[4,22] This is consistent with the formation of cracks during the delithiation as observed by operando optical microscopy in Video S1 and S2 and in previous work.[23] This is due to the constraint imposed by the current collector in the x and y (in plane) directions against the electrode retraction. In these directions, the electrode is strongly contracting, but the Cu CC does not. This leads to large deformation incompatibilities in the x and y directions while the electrode is not constained in the z (out of plane) direction. This is the reason why the cracks are occurring in planes perpendicular to the electrode. A study by X-Ray tomography of the standard (Zn-free) electrode showed that cracks preferentially initiate from porosity (which is equivalent to a flaw) at the bottom of the electrode near to the current collector interface, then propagate first in the z direction (toward the top of the electrode), then grow in the x-y plane.[23] Although SEM observations of cracks presented in Figure S2 show that the cracks do not reach the Cu CCs irrespective the formulation or Cu CC type, cracks could be kinking out of their initial propagation direction during their growth.[4] Subsequent observations by X-ray nanotomography of the entire thickness of these electrodes, which we hope will provide a final answer to this question, will be revealed in a future article. From Figure 2, the spacing between adjacent and parallel cracks (equivalent to the island dimensions) were estimated for the six formulation and CC pairs over several regions of interest (each ROI's surface is equal to 0.4 mm^2) and the results are displayed in Table 2.

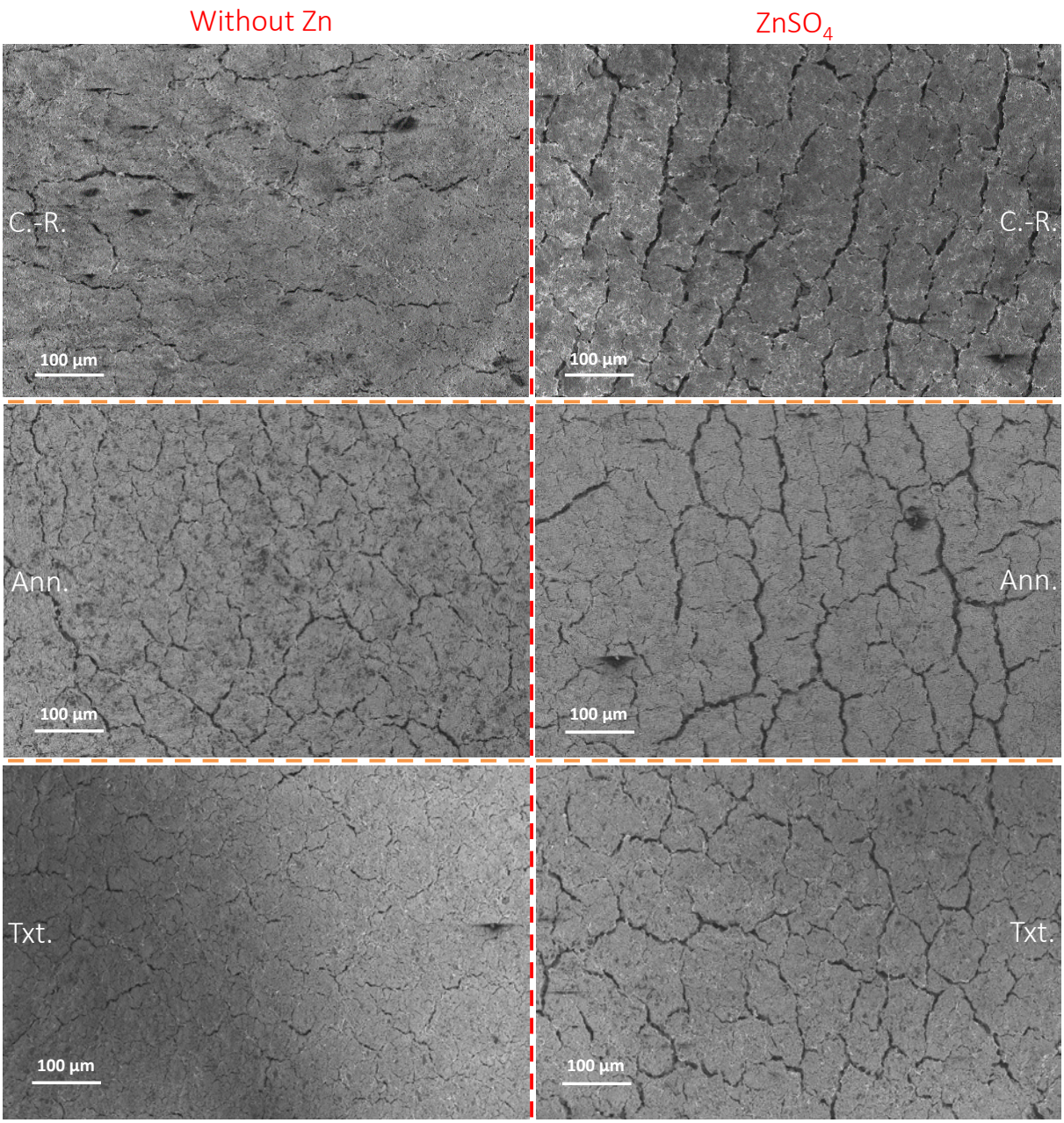

Figure 2. SEM observations of electrodes surfaces after 1 cycle; Left side from top to bottom: Zn-free formulations (21.4% SF) with C.-R., then Ann., and finally Txt. Cu CC; Right side from top to bottom $ZnSO_4$ formulations (22.3% SF) with C.-R., then Ann., and finally Txt. Cu CC. For the Ann. and Txt. Cu CC electrodes, the brightness and contrast were adjusted with the software ImageJ.

The crack spacing is rather similar for the $ZnSO_4$ formulation on all three Cu CCs with mean values between 74 and 84 µm. This can be correlated to their similar electrochemical performance, as seen in Figure 1. At first sight, this seems to indicate that the $ZnSO_4$ formulation electrode cracking is primarily controlled by its mechanical properties and not by

the Cu CC. In fact, electrodes made with a cross-linked binder have shown superior mechanical strength with higher resistance to indentation and scratching than the reference electrodes.[16,17] Therefore, the higher cohesion of such an electrode could explain why the grade of the Cu CC has no major impact on the mechanical and electrochemical properties for the $ZnSO_4$ formulation. In contrast, for the Zn-free formulation, the mean crack spacing on the C-R CC (98 µm) is about twice that of the Ann. CC (55 µm) and three times that of the Txt. CC (37 µm). As such, the electrode cracking depends on the interface between the electrode film and the Cu CC, and thus strongly on the aspect of the CC for this formulation. We may note that the samples with $ZnSO_4$ show larger cracks, likely because the islands are bigger, such that during the delithiation the overall retraction length is higher. Larger cracks could be beneficial for power applications, but galvanostatic cycling at high C/rate to verify this assumption was not performed yet.

Table 2. Electrode crack spacing (equivalent to the island dimension) for the $ZnSO_4$ (22.3% SF) and its Zn-free reference (21.4% SF) formulations with either C.-R., Ann. or Txt. Cu CC.

		Spacing between cracks [µm]	Std. Dev. [µm]	Number of measurements (Nb. of ROIs)	Film thickness [µm]
$ZnSO_4$	Cold rolled	84	18	44 (2)	33
	Annealed	81	24	162 (4)	38
	Textured	74	21	260 (6)	33
Without Zn	Cold rolled	98	35	28 (2)	33
	Annealed	55	18	208 (5)	29
	Textured	37	15	214 (6)	29

To gain a better understanding of these phenomena, the Cu CCs were characterized through nano-indentation experiments, profilometry and XPS spectroscopy. Nano-indentation and profilometry results are displayed in Table 3. The Cu CCs used present a relatively narrow range of elastic modulus (*E*) with 100, 90 and 70 GPa for the C.-R., Ann., and Txt. Cu CCs, respectively. However, there is a stark difference in terms of hardnesses (*H*), which are equal to 2, 1 and 1.3 GPa for the C.-R., Ann., and Txt. Cu CCs, respectively. This parameter can be used to determine the yield strength (*YS*) and ultimate tensile strength (*UTS*) of the CC with fairly good accuracy as they are linearly correlated.[24] To do so, the hardness is first converted to the Vickers hardness number (*VHN*) using Equation 1[25]:

$$VHN = H \times \frac{1000}{9.81} \quad (1)$$

Then, applying Equation 2 and 3 for respectively the *YS* and *UTS*[24]:

$$YS = 2.874 \times VHN \text{ [MPa]} \quad (2)$$

$$UTS = 3.353 \times VHN \text{ [MPa]} \quad (3)$$

These equations were obtained by a linear regression analysis over 120 data points from copper alloy samples.[24] The validity range of those equations span from 50 to 425 *VHN*, which covers our data range (see Table 3). Results in Table 3 show that the calculated yield strength and the ultimate tensile strengths for the Ann. Cu CC are 2 times lower, and for the Txt. Cu CC, 1.5 times lower than for the C.-R. Cu CC. The capacity retention for the Zn-free electrodes increases when the yield strength of the current collector decreases, *i.e.* when its deformability increases, while for the electrode with $ZnSO_4$, the cyclability is independent of the mechanical properties of the collector. These trends are depicted in Figure 3a where the capacity retained at the 60th cycle is plotted as a function of the yield strength of the Cu CC.

Table 3. Main mechanical characteristics and roughness, average (*Ra*) and quadratic average (*Rq*) of the C.-R., Ann., and Txt. Cu CC. The mean roughness values and their standard deviation were determined from 6 measurements over a distance of 2 mm for each Cu CC.

Current collector	Elastic modulus [Gpa] (Measurement depth [µm])	Hardness [Gpa] (Measurement depth [µm])	Vickers hardness number	Yield strength [MPa]	Ultimate tensile strength [MPa]	*Ra* [nm]	*Rq* [nm]
Cold rolled	100 (0.3)	2 (0.6)	204	586	684	45 ± 4	60 ± 6
Annealed	90 (0.2)	1 (0.3)	102	293	342	193 ± 4	266 ± 13
Textured	70 (0.3)	1.3 (1)	133	381	444	389 ± 14	479 ± 25

Figure S3 shows SEM images of the different Cu CCs surface over a distance of about 20 µm and their respective roughnesses over a distance of about 400 µm. The appearance of the roughness is similar for the C.-R. and Ann. Cu CCs, as can be seen respectively in Figure S3a and S3c, and takes the form of parallel stripes, most likely coming from the lamination process. However, the roughness measurements show that the amplitude of those stripes are much higher, but they are less frequent for the Ann. Cu CC (Figure S3d) as compared to the C.-R. Cu CC (Figure S3b). The Txt. Cu CC presents a completely different roughness in the form of grains (Figure S3e), which results in a roughness profile with high amplitude and high frequency, as can be seen in Figure S3f. Unfortunately, the texturization method for the Txt. Cu

CC is not provided by the supplier. Quantitative values of roughness were obtained from Figure S3b, S3d and S3f for the different Cu CCs and are given in Table 3. The average (*Ra*) and quadratic average (*Rq*) roughness is approximately 4 times higher for the Ann. than for the C.-R. Cu CC and around 2 times higher for the Txt. than for the Ann. Cu CC. Interestingly, the standard deviation is at most around 10% for the *Ra* or *Rq* value of the different Cu CC, meaning that their roughness is rather homogeneous over their whole surface. The relation between the cracks spacing and the roughness of the Cu CC is shown in Figure 3b. It is observed that this cracking mechanism of the electrode is relatively independent of the roughness of the Cu CC in the case of the $ZnSO_4$ containing electrodes. On the contrary, the cracks spacing clearly appears to decrease with the increase in the roughness of the Cu CC for the Zn-free electrodes. These trends suggest again that the $ZnSO_4$ containing electrodes' damage mechanisms are independent of the substrate properties and thus, are controlled by the electrode cohesion, while for the Zn-free electrodes these damage mechanisms depend on the interface between the electrode and the Cu CC.

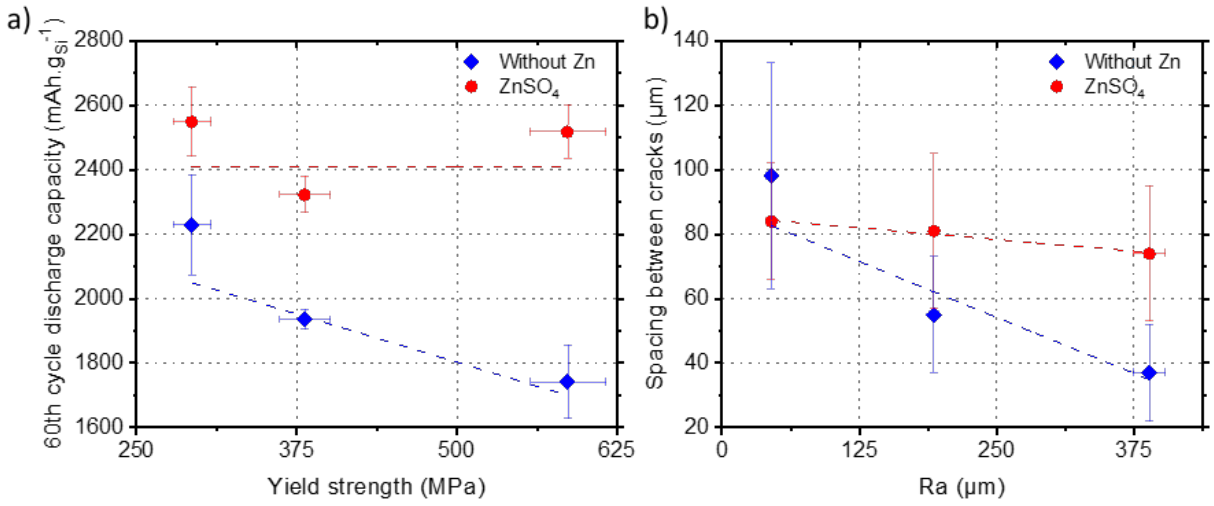

Figure 3. (a) 60th cycle specific discharge capacity as a function of the Cu CC yield strength for both formulations; (b) Spacing between cracks as a function of the average roughness for both formulations. Dotted lines are linear regression plotted only for ease of interpretation.

The chemical compositions of the surfaces of the different Cu CCs were investigated by X-Ray photoelectron spectroscopy (XPS) and are presented in Figure S4 (with peaks positions available in Table S3). The surface composition of the C.-R. and Ann. Cu CCs are similar, composed of a layer of $Cu(OH)_2$ and Cu_2O, whereas the surface of Txt. Cu CC is composed of $CuCr_2O_4$. Nevertheless, even if the compositions are different, the surface of the CC always contains Cu(II) cations, which can form copper carboxylate bonds with the binder,[16] thus

favoring the adhesion between the film and the Cu CC. It is therefore difficult to rationalize the difference of behavior exclusively by the composition of the interface.

To summarize, the Zn-free formulation electrodes' cyclability and fracture behavior show a significant dependence on the Cu CC grade. On the contrary, such a dependence is not noted for the Zn cross-linked electrodes, which have a much higher cohesion.[17] Therefore, for the reference formulation of lower cohesion, it appears that the increase in adhesion at the CC's interface via the roughening of the surface of the current collector and/or the decrease of its yield strength contribute to mitigate the electrode film's mechanical damage, therefore preserving its cyclability.

One way to modulate the adhesion at the interface as well as the mechanical properties of the collector in contact with the electrode is to cover the surface of the collector with a buffer layer. Using this technique, Xu et al.[7] and Li et al.[8] showed that the insertion of a soft and conductive layer of conductive carbon and PVDF is beneficial to the cyclability of silicon-based electrodes. The more conventional approach is to increase the roughness of the current collector.[11] However, the benefit of this approach decreases when the binder content in the electrode (*i.e.* its cohesion) increases, as shown by Jeon et al.,[9] which is reflected by the Zn cross-linked electrodes with higher cohesion. On the contrary, Basu et al.[10] observed that the addition of a conductive layer, which also promotes the sliding of the silicon electrode, can bring about a noteworthy improvement in the cyclability of silicon-based electrodes. Results from both literature and this study point to an urgent need to comprehensively and systematically study the impact of the surface properties of the CC and the CC-coating interface on the mechanical and electrochemical behavior of electrodes, particularly when the active material presents volume variations with the insertion and desertion of lithium.

2.2. Ink solid fraction modification and its influence on electrode properties

As mentioned in the introduction, the ink SF influences its rheological properties and consequently its homogeneity during the mixing, casting, and drying stages. Figure 4 shows the viscosity as a function of the shear rate for the Zn-free and $ZnSO_4$ inks at different SFs. The inks exhibit a shear-thinning behavior, which means that the viscosity decreases with increasing shear rate. The viscosity of the ink increases with the solid fraction, mainly because the solvent volume is reduced such that particles interactions are favored. This makes the SF adjustment a simple way to tune ink viscosity without modifying the electrode formulation. Interestingly, both formulations have similar viscosity at the tape casting shear rate of either 37 or 56 s^{-1} (*i.e.* at the blade gaps h = 150 or 100 µm, with a casting speed of 5.6 $mm.s^{-1}$). Therefore, both

formulations should show comparable behavior under the blade gap during electrode preparation. At a shear rate of 0.01 s^{-1}, *i.e.* nearly in rest condition, the $ZnSO_4$ formulation ink viscosity is always slightly inferior no matter the SF (see Figure S5b). This could originate from a denser binder adsorption on the silicon particles, which reduces steric hindrance and liquid phase viscosity, or from an increased interparticle electrostatic repulsion induced by $ZnSO_4$ salt adsorption at the surface of the particles.

Similar studies were conducted for inks formulated with ZnO as well as its associated Zn-free references (see Table S4 for composition). Corresponding results are shown in Figure S5a. This same behavior is also observed for the inks formulated with ZnO and its reference, independently of the SF, as can be seen in Figure S5a. However, the magnitude of this effect is much larger than with the $ZnSO_4$ precursor. Generally, the ink viscosity above 22% SF for the ZnO and its reference formulation is higher than that of the $ZnSO_4$ and its reference, as is summarized in Figure S5b. This highlights that there is a complex interplay between pH, concentrations of each component, and presence of divalent cations. Such complexity was previously identified in binder solutions.[17]

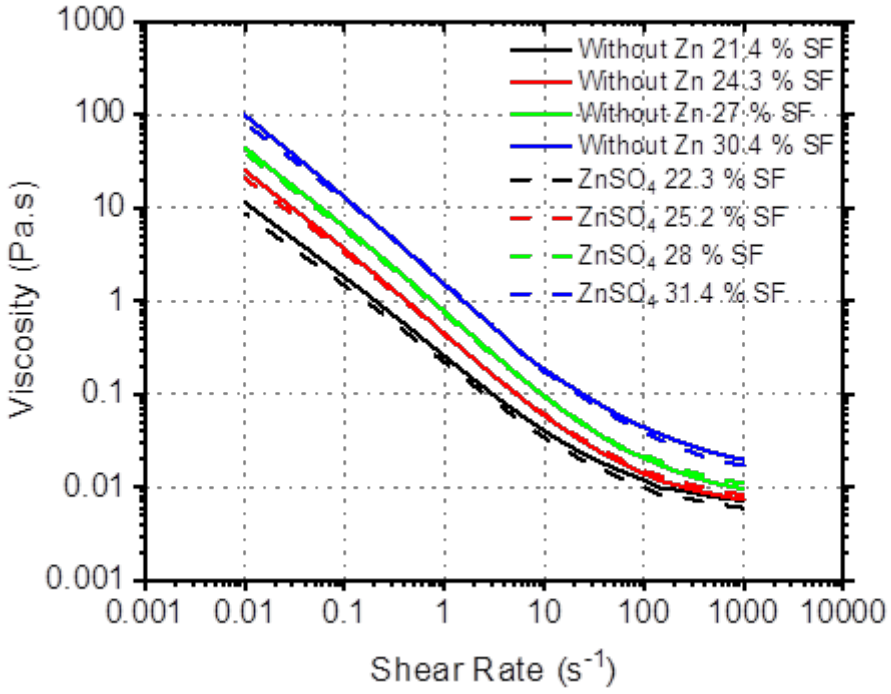

Figure 4. Viscosity as a function of shear rate for inks without Zn or with $ZnSO_4$ at different SF.

The ink yield stress as well as storage (*G'*) and loss (*G''*) moduli are gathered in Table 4 for the Zn-free and $ZnSO_4$ formulations of different SFs. The former represents the minimal stress required for the fluid to flow and is obtained by multiplying the viscosity by the shear rate at the first measurement point, around 0.01 s^{-1}. For both formulations, the yield stress increases with the SF, up to 9-fold from the lowest (21.8%) to the highest (27.5%) SF. This increase is even more marked for the ZnO and respective reference formulations, as the yield stress reaches 3.54 Pa at high (27.1%) SF (a 17-fold increase). All data are summarized in Figure S5c. The yield stress is associated with ink stability during drying (at rest), such that the higher the yield stress, the less prone the ink is to sedimentation and phase segregation. As such, increasing the SF reduces those risks.

Table 4. Yield stress, storage modulus, and loss modulus for inks without Zn or with $ZnSO_4$ at different SFs.

	Zn-free				**$ZnSO_4$**			
Solid fraction [$_w$%]	21.4	24.3	27	30.4	22.3	25.2	28	31.4
Yield stress [Pa]	0.11	0.25	0.44	0.98	0.09	0.2	0.38	0.81
Storage modulus [Pa]	3	28	54	193	1.8	15	42	120
Loss modulus [Pa]	0.8	10	20	88	0.6	6	15	62

The *G'* and *G''* values are taken from their plateau at low strain amplitude (not shown) for a 1 Hz solicitation frequency. For both formulations at every SF, *G' > G''*, which proves that the ink behaves as a physical gel, *i.e.* there is interconnected matter throughout the whole volume. The storage modulus increases with SF, *i.e.* the matter network in the ink fortifies, which is consistent with the yield stress evolution with SF.

In conclusion for these measurements, it appears that the viscosity of the ink at high shear gradient is sufficiently low to allow good homogenization, and its physical gel nature at quasi-rest ensures the stability of the ink, thus maintaining its homogeneity immediately after casting and at the start of drying. The differences in the rheological behaviors of both formulations are low.

In order to evaluate the effect of the SF on the magnitude of silicon particles/binder interactions[26] thermogravimetric analyses (TGA) of silicon particles after being in contact with

the binder solution were carried out. The inks for these analyses were prepared with a binder:Si mass ratio of 8:1 (for comparison the ratio is 1:8 in the ink formulations used to manufacture the electrodes) in order to maximize the adsorption of the binder and thus facilitate its detection by TGA. Si particles were suspended in the binder solutions, recovered by centrifugation, then dried at room temperature, and again at 60 °C (see supporting information for details). Figure 5 illustrates the mass loss of dried Zn-free or $ZnSO_4$ binders on silicon particles prepared at different SFs (averaged from 3 measurements). The first mass loss from 30 to 150 for the Zn-free and 160 °C for $ZnSO_4$ samples respectively, is associated with dehydration. This mass loss is between 0.9 and 1.2% for the Zn-free samples at 21.4 and 27% SF, respectively. For the $ZnSO_4$ samples, the mass loss is 1.4 and 2.3% at 22.3 and 28% SF, respectively. The second mass loss is associated with the decomposition of the organic moieties and spans between 150 and 340 °C for the Zn-free samples, and between 160 and 450 °C for the $ZnSO_4$ samples. This mass loss is 3.9 and 4.6% for the Zn-free samples at 21.4 and 27% SF, respectively. For the $ZnSO_4$ samples, the mass loss is higher, at 5.7 and 8.2% for 22.3 and 28% SF, respectively.

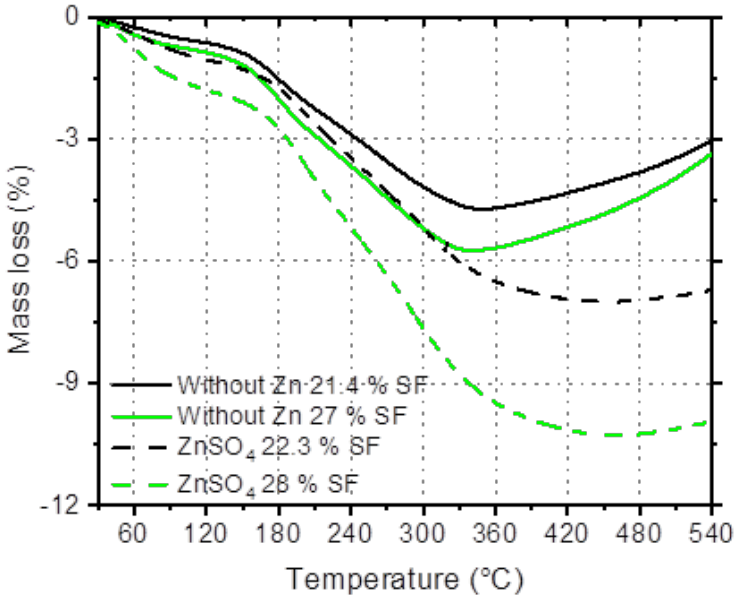

Figure 5. Mass loss *vs.* temperature of silicon particles covered by dried binder, either without Zn or with $ZnSO_4$, at different SFs (experiments carried out in air).

Irrespective of the SF, the mass loss related with the organic component is higher for the $ZnSO_4$ binder. The fact that more binder is readily adsorbed on the particles in the ink suggests a higher affinity with the Si particles. The CMC and citric acid are adsorbed to the silicon particles through Van der Waals interactions, and/or hydrogen or ionic bonds.[27–29] The

Zn(II) cations are expected to adsorb to the silicon particle surfaces through electrostatic interactions. The presence of Zn(II)-carboxylate coordination bonds in the $ZnSO_4$ formulation should causes more binder to be retained on the particles. Further, the amount of binder ad/absorbed increases with the SF because as the liquid volume is reduced, the binder/particles interactions are favored. The difference in binder adsorption between both formulations could explain the viscosity difference seen in Figure 4 under the hypothesis of lower ink liquid phase viscosity being favored due to enhanced ab/adsorption in the presence of Zn(II). Interestingly, the silicon oxidation, which appears as a mass gain at high temperature, is delayed by around 110 °C with the $ZnSO_4$ binder compared to the Zn-free binder (around 440 and 330°C, respectively). This delay in the silicon oxidation might reflect a better silicon coverage by the binder. Indeed, the carbonization of the binder layer may prevent the direct contact between the silicon surface and the air until it is oxidized as CO_2. Importantly, the "spontaneous" binder adsorption on the particles in the ink only represents around 4 to 8 $_w$% (for a binder volume 8 times higher than in a typical ink formulation), whereas the binder proportion in the electrode is around 15 to 20% (as can be seen in Table 1). Therefore, most of the binder is dissolved in the ink liquid phase rather than being readily adsorbed of the silicon and deposits at the particle surface and interparticle junctions during the drying step.[30]

The electrical resistivity of the Zn-free and $ZnSO_4$ electrodes at different SFs is illustrated in Figure 6 (for electrodes deposited on insulating Mylar rather than conducting Cu). The $ZnSO_4$ coating resistivity is higher than the Zn-free ones, independent of SF. The electrical conductivity of composite electrodes made with active material, conductive additive, and binder has a first-order dependence on the binder layer thickness adsorbed between the conductive additive particles[31,32] because the electric conduction is made by tunneling (once the electric percolation is achieved in the electrode, *i.e.* above a critical volume fraction of conductive additive, which is the case for these electrode formulations). Thus, in agreement with the picture coming out from the TGA measurements, the $ZnSO_4$ binder might also be more adsorbed on the graphene particles. Another cause could be the trapping of electrons (negatively charged) or the hindering of their transfer through and between graphene particles due to their attractive interaction with the adsorbed Zn^{2+} cations (positively charged).[33] Additionally, the resistivity increases with the SF; this is again in agreement with the increase of the amount of adsorbed binder on the Si particles with increased SF (Figure 5), as the trend will be similar for the binder adsorption on graphene. The electrode conductivity is quite low, only around one order of magnitude higher than the ionic conductivity of the electrolyte (LP30 conductivity is 0.015 $S.cm^{-1}$ at 20 °C[34]) for the Zn-free electrodes and approximately the same order of magnitude

for the $ZnSO_4$ electrodes. This could induce non-negligible impedance from the conductive additive networks, as compared to the electrolyte.[35] Fortunately, upon silicon lithiation, its electric conduction increases by several orders of magnitude,[36] reducing the impedance of the electrode as a whole. Although the presence of conducting additive is necessary, previous work[37] showed that it is possible to reduce the conducting carbon content down to 6 $_w$%, which increases the resistivity to about 400 Ohm.cm, without suffering any increase in the electrode resistance nor decrease in cyclability.

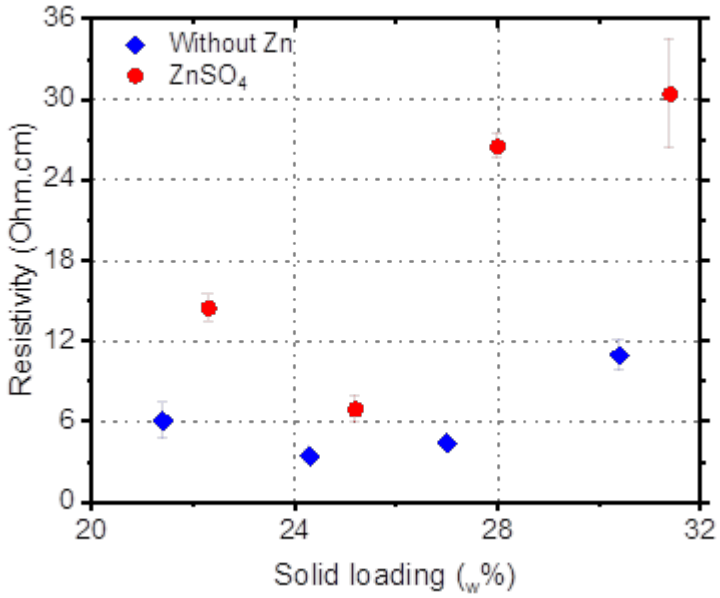

Figure 6. Electrode coating (without Cu CC) resistivity for Zn-free and $ZnSO_4$ formulation at different SF.

Figure 6a to 6d present the specific discharge capacities and CEs of the formulations with $ZnSO_4$ at 22.3 and 28% SF and Zn-free formulations at 21.4 and 27% SF, all with a C-R Cu CC. When a higher SF is used, both the capacity retention and CE are enhanced for both formulations. The performance enhancement is however much more significant for the Zn-free formulation. Namely, for the latter, the 60th cycle capacity is approximately 2470 *vs.* 1740 mAh.g_{Si}^{-1} and the 1st cycle CE is 87.0 *vs.* 81.1%, for the 27 and 21.4% SF, respectively. For the $ZnSO_4$ formulation, the 60th cycle capacity is approximately 2550 *vs.* 2520 mAh.g_{Si}^{-1} and the 1st cycle CE is 86.9 *vs.* 84.5% (though within std. dev. range), for the 28 and 22.3% SF, respectively. The average CE between the 20th and 65th cycle was not compared because the CE was over 100% for most of the cycles, purportedly due to parasitic reactions at the Li counter-electrode during the charge.

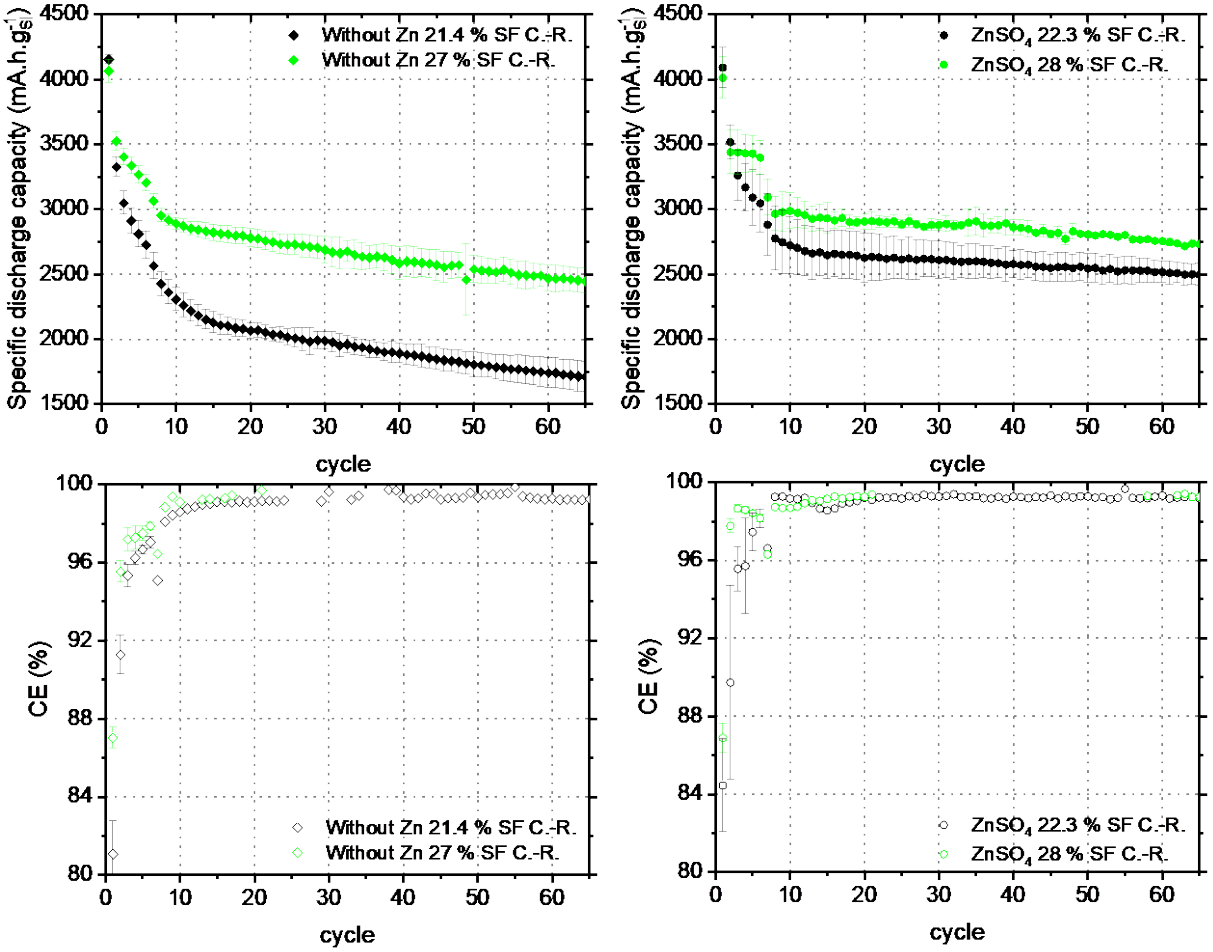

Figure 7. Mean specific discharge capacities and CEs as a function of cycle number for electrodes prepared with different ink SFs, cast on C.-R. Cu CC: (a, c) Zn-free formulation; (b, d) $ZnSO_4$ formulation. The electrodes were cycled at C/40 for the 1st cycle, then C/20 for 5 cycles, and C/10 for the remaining cycles. The mean values and their standard deviation were determined from a minimum of 3 electrodes for each formulation.

It clearly appears that increasing the SF improves the electrochemical performance of both formulations on C.-R. Cu CC. The difference is particularly visible for the Zn-free formulations, so these were further characterized (as well as the Zn-free + LiOH formulation with a C.-R. Cu CC, as can be seen in Figure S6). First, the binder distribution on particles could be modified by the SF, as is suggested by the enhanced adsorption of binder on particles with increasing SF. However, preliminary 3D analysis of electrodes by focused-ion beam (FIB)-SEM was not conclusive because the binder was barely discernable. Second, phase segregation and binder accumulation on top of the electrode[12,13] may occur at 21.4% SF considering the rather low value of the ink yield stress. EDX quantification was used to evaluate

the binder distribution (through the analysis of Na/K). Values below one percent were obtained. EDX quantifications of Na/K at the electrode surface render similar atomic percentage (within std. dev. range) for both Zn-free 21.4% SF and 27% SF formulations, suggesting that the distribution of the binder may not vary with the SF. This conclusion should however be taken with caution, because the underlying hypothesis is that the Na and K ions (introduced with the CMC and the citric acid buffer) are localized in the polymer phase, as a counter ion of the carboxylates of CMC and citric acid. However, these functions can be involved in bonds with the surface of the silicon or be neutralized, in the form of carboxylic acid functions. Then, Na^+ and K^+ ions can simply be adsorbed on the surface of the silicon, therefore not reflecting the exact distribution of the binder. Further, Cu EDX quantification at the coating/Cu CC interface shows similar atomic percentage (not shown) for both Zn-free formulations, suggesting similar extent of corrosion and of subsequent induced reticulation by copper ions.[16] We therefore believe the more likely explanation for the superior electrochemical performance at higher SF is due to the enhanced adsorption of binder on silicon particles with increasing SF.

In fact, the CE during the first cycles is clearly improved for both formulations (see Figure 7 and the corresponding text). The CE in the early cycles is influenced both by the formation of the SEI and by the mechanical degradation of the electrode microstructure. The irreversible capacity associated with this first phenomenon results from the reduction of electrolyte species, while that which is associated to the second results from a loss of connectivity of the active mass with the current collector. The binder plays the role of an artificial SEI by minimizing the direct contact between the silicon surface and the liquid electrolyte, which reduces its degradation at low potential.[15,38] Increased coverage of the silicon particles surface at higher SF is therefore a likely explanation for the CE improvement. It is possible to analyze the contribution of the binder as an artificial SEI through the incremental capacity curves. Indeed, we have shown that the intensity of the reduction peak(s) of the electrolyte species, between approximately 0.4 and 1V, *i.e.* before the silicon lithiation occurs, is indicative of the modulation provided by the binder deposited on the surface of the active material against the degradation of the electrolyte. The more binder coverage, the less the electrolyte is degraded.[39,40] Figure S7 presents the incremental capacity curves of the first discharge in the 0.4-1.4 V potential window for Zn-free formulations prepared at the SF of 21.4% and 27% on the C.R. Cu CC. It can be clearly observed that the electrolyte reduction peak is markedly attenuated when the SF is higher. The same observation can be made for the Zn-free + LiOH formulation. This result indicates a better coverage of the surface of the silicon by the binder when the SF increases, in accordance with a greater adsorption on the surface of

the silicon. The enhanced adsorption of the binder on the silicon particles could also be at the origin of the superior electrode mechanical stability by enhancing the mechanical bridging of the particles.[41] Overall, the important result here is that the SF should be tuned to maximize the electrochemical performance of silicon-based electrodes.

Interestingly, the electrochemical performance enhancement with the Ann. And Txt. Cu CCs do not seem systematic at higher ink SF. Indeed, increasing SF to 27 and 28% for the Zn-free and $ZnSO_4$ formulations, respectively, yielded scarce (as shown in Figure S9) or even no improvement (Figure S8). As such, that the interplay between both SF and Cu CC influence parameters still needs to be better understood to systematically improve the electrochemical performance of silicon electrodes. Nevertheless, these results attest once again to the Zn cross-linked electrodes' superiority, which have electrochemical performances nearly independent of the Cu CC grade and ink SF, all the while remaining superior to that of non-reticulated electrodes.

3. Conclusion

The influences of the grade of copper used as current collector and of the solid fraction in the ink were evaluated for a negative electrode of a Li-ion battery rich in silicon and formulated with the binder CMC/citric acid, crosslinked or not through the addition of Zn(II) cations. The mechanical behavior during cycling and the cyclability of the reference electrode based on the non-crosslinked binder are significantly influenced by the choice of current collector and the ink solid fraction. The choice of a current collector with a lower plasticity threshold, *i.e.* more deformable, and/or rougher surface significantly modifies the cracking mechanism of the electrode in the first cycle and increases the electrode capacity retention. The increase in the solid fraction also considerably increases the cyclability of this electrode, which can be partly attributed to the increased amount of binder that adsorbs on the surface of the active material in the ink. This results in a better coverage of the surface of the active material, which leads to a minimization of the degradation of the electrolyte during the first cycle. The stronger absorption of the binder could also be at the origin of a better mechanical behavior of the electrodes. The electrode formulated with the crosslinked binder is less sensitive to the choice of the current collector and the solid fraction of the ink. The cracking mechanism of the electrode during the first cycle and the cyclability are almost invariant. In all cases, the electrochemical performance is increased by the crosslinking of the binder. This formulation principle, which consists of adding a metallic cation capable of cross-linking a polymeric binder via the formation of coordination bonds, therefore appears to be very effective, making it

possible to obtain robust formulations which are not as sensitive to the manufacturing conditions of the electrodes and the nature of the grade of copper used as current collector. This allows for better reproducibility and manufacturing quality of the electrodes. For both parameters (SF and grade of the copper used as current collector), the mechanisms that affect the electrochemical performance are complex, multifactorial and not yet fully rationalized. Nevertheless, in light of possible performance differences, these parameters should be more systematically addressed in the field of battery research.

4. Experimental Section/Methods

4.1 Material preparation

Binder solutions:

First, a pH 3 buffer solution (0.171 M of citric acid + 0.084 M of KOH or NaOH) was prepared by dissolving citric acid (99%; Sigma-Aldrich) and KOH or NaOH salt (> 98%; Sigma-Aldrich) in ultra-pure water. Then, 5 mL of buffer plus a variable amount volume of ultra-pure water was used to dissolve 160 mg of NaCMC (Mw ≈ 700 000 g.mol^{-1}, D.S. 0.9; Sigma-Aldrich). The as-obtained solution was the reference binder solution ($Zn/RCO_2H = 0$). Finally, upon NaCMC complete and homogeneous dissolution, the Zn(II) precursor was added all at once, and left until homogenization. For the reference containing LiOH, $LiOH•H_2O$ (≥ 98%; Sigma-Aldrich) was also added at once. For every step, solutions were magnetically stirred at room temperature.

The salts coordination water was counted as a part of the binder water volume, whereas the approximately 15 $_w$% ad/absorbed water in NaCMC was not taken into account.

For this study, different precursors of Zn(II) were used: $ZnSO_4•7H_2O$ (Pure cryst.; Alfa Aesar), (99.99%; Alfa Aesar) and ZnO (99.99%; Alfa Aesar). Their quantity was adjusted to systematically reach the predefined theoretical molar coordination ratio of 0.22:

$$Coordination\ ratio = \frac{n_{Zn}}{n_{COOH(citric\ acid+CMC)}} \quad (5)$$

Electrodes:

The Si powder used as active material was obtained by ball-milling Si powder (325 mesh, 99.96%; Materion) using a HD-01 attritor (Union Process). The milling was performed under argon atmosphere for 20 h at 600 rpm with a ball-to-powder mass ratio of 10:1. The as-milled Si powder was composed of micrometric agglomerates of secondary particles (d_{50} ≈ 10 µm, S_{BET} ≈ 20 m².g^{-1}) and primary particles were under the micron. Its oxygen content determined by a LECO analyzer was approximately 1 $_w$%.

160 mg of Si powder, 24 mg of graphene platelets used as conductive additive (xGnP M15 grade from XGSciences, average thickness ≈ 7 nm, average diameter = 15 µm, surface area ≈ 120-150 $m^2.g^{-1}$, according to supplier data) and a variable volume of binder solution (by weight) were set in a vial with three balls (diam. = 9.5 mm), both made of silicon nitride. The whole was mixed using a Pulverisette 7 (Fritsch) planetary mixer for 1 h at 500 rpm. Then, the as-prepared ink was tape casted with a doctor blade on a Cu current collector (Cu CC), either cold-rolled (C.-R.) (99.9%, thickness ≈ 20 µm, cold rolled; PI-KEM), annealed (Ann.) (99.8%, thickness ≈ 25 µm; Alfa Aesar) or textured (Txt.) (thickness ≈ 14 µm; no supplier data available). For the Txt. Cu CC, the ink was tape casted on the textured side (the other side is flat). The blade gap was h = 150 µm (model 3540, s = 5.6 $mm.s^{-1}$; Elcometer) or h = 100 µm for the inks having a 27% SF, or higher in order to obtain the desired silicon loading (see below). As-prepared films were dried at room temperature for 12 h. Finally, electrodes were punched (diam. = 1 cm) and dried for 2 h at 100 °C under vacuum (P ≈ 10 mbar) prior to mass (Δm = ± 0.01 mg; OHAUS) and thickness (Δe = ±1 µm; Mitutoyo) measurements. Then, they were dried again for 1 h under the same conditions prior to assembly. Electrodes were selected if their active mass loading reached 1.75 ± 0.1 $mg_{Si}.cm^{-2}$.

Solid fraction:

The ink dry matter percentage, as defined by Equation 6, corresponds to the ink solid fraction (SF):

$$SF = \frac{m_{dry}}{m_{dry}+(V_l \times \rho_{H2O})} \times 100\ [_w\%] \quad (6)$$

With m_{dry} (mg) the total mass of the dry components used for the composite electrode, *i.e.* the active material, the graphene, and binder. The solvent mass (*i.e.* water) is calculated by multiplying V_l (ml) the binder volume used for the ink, by ρ_{H2O} the water density which is equal to 997 $mg.mL^{-1}$. The SF is modified by changing the binder solution concentration and volume used for the ink formulation. As the binder solution is more concentrated at higher SF, a lower volume of binder solution is added for the slurry making such that the weight percentage of all elements in the electrode composition remains constant for each SF. For example, a standard binder solution contains 8.2 mL (5 mL of CMC/buffer plus 3.2 mL of ultra-pure water), and 0.8 mL of that binder solution is used for the ink formulation. The corresponding SF are 21.4 and 22.3% for the Zn-free and $ZnSO_4$ formulation, respectively, with the difference coming from the addition of $ZnSO_4$. To obtain a higher SF, the binder solution volume is set to 5.13 mL (5 mL of CMC/buffer plus 0.13 mL of ultra-pure water), and then 0.5 mL of binder solution is used for the ink formulation. The corresponding SFs are 30.4 and 31.4% for the Zn-free and $ZnSO_4$ formulation, respectively.

4.1 Material characterization

XPS:

XPS spectra were recorded using an AXIS Ultra (Kratos) equipped with an Al monochromatic source ($E_{K\alpha}$ = 1486.6 eV). The pass energy was fixed to 20 eV to measure the regions of interest, allowing a 0.1 eV resolution. The C 1s signal from adventitious carbon was used for energy calibration, setting its position at 284.8 eV. For reproducibility, 14 measurements were performed per ROI's energy range (Cu 2p, Cu LMM) for each Cu CC sample, and the spectra were summed. For the Txt. Cu CC the rough side was analyzed.

SEM:

The surfaces and coating-CC interfaces of the electrodes (after removal with adhesive tape) were coated with carbon to increase their conductivity, then analyzed with an EDX SDD probe (SAMx) in a SEM 5800LV (Jeol) with a voltage and gun current of 15 kV and 0.5 nA.

CC surface images are obtained using a SEM JSM 7600F (Jeol) with an in-lens SE detector. The gun voltage was 5 kV. For the Txt. Cu CC, the rough side was analyzed.

Electrodes surface images are obtained after one cycle using the SEM of a FIB-SEM 550 L (ZEISS) with the in-lens SE detector. The gun voltage and current were 6 kV and 5 nA. To avoid any air exposure, a sealed sample transfer shuttle (SEMILAB) was used between the glove box (where the cells were dismantled) and the FIB-SEM.

Profilometry:

The current collectors' surface roughnesses were measured using a stylus profiler P-7 (KLA) using a diamond tipped stylus with a radius of curvature of 2 µm. For the C.-R. and the Ann. Cu CC, the stylus was passed orthogonally to the stripes direction because of their preferred orientation. For these, the stylus load was 2 mg, and 0.5 mg for the Txt. Cu CC. In all cases, the stylus was passed six times over 2 mm (for the sake of reproducibility, the results were averaged) at a speed of 100 µm.s^{-1}. The sampling rate was 1 kHz. For the Txt. Cu CC, the rough side was analyzed.

Rheology:

Electrode ink flow properties were determined with a MCR101 (Anton Paar) rheometer. The geometry used was plane-plane configuration (upper plate diam. = 50 mm, gap between both plates h = 300 µm). The temperature was regulated to 20 °C with a Peltier probe. Storage (G') and loss (G'') moduli were measured with increasing strain from 0.01 to 100% at a frequency of 1 Hz. Shear stress and viscosity were measured with increasing shear rate from

0.01 to 1000 s^{-1} and then back down to 0.01 s^{-1}. The back scan was taken for the ink viscosities as tape casting occurs after the high-shear planetary mixing step.

TGA:

The amount of ab/adsorbed binder on the surface of the silicon particles was evaluated using a thermo-gravimetric analysis. Inks containing 80 mg of silicon plus 3.2 mL of binder solution were prepared identically to those used for the coatings, with the exception of the number of silicon nitride balls placed in the jar for planetary mixing (which was increased to 6 instead of 3). Additional samples were made with 2.36 mL of more concentrated binder solution to increase the SF. In fact, the binder:Si mass proportion was selected to be 8:1 contrarily to classic ink formulation, for which the proportion is 1:8. Next, the inks were centrifuged in a glass vial for 5 min at 5000 rpm^{-1}. The supernatant fluid was removed and the remaining powder was allowed to dry, first for 12 h at room temperature and then for 12 h at 60 °C. Finally, the samples were analyzed with a STA 449F3 Jupiter (NETZSCH) between 30 and 540 °C at 5 °C.min^{-1} under air. For reproducibility, 3 measurements were performed per formulation.

Indentation:

The mechanical properties of the Cu current collectors were analyzed using a nano-indenter NHT^3 (Anton Paar). The system coupled a sinusoidal load to the standard load to render a hardness and elastic modulus depth profile. The head (Berkovich) applied a maximum force from 0.1 to 400 mN. The oscillating contribution amplitude was 5% of the force at any given time, and a frequency of 5 Hz and an acceleration coefficient (CSR strength ramp) of 0.1 s^{-1} were used. The Oliver and Pharr method[42] was used to determine the hardness and elastic modulus. For the latter calculus, the Poisson coefficient was taken to be 0.33. Nine measurements were performed for each sample for the sake of reproducibility. For the Txt. Cu CC the face presenting the flat surface was analyzed.

Conductimetry:

The electrical resistivity of the electrode coatings was measured with a 280SI 4-point measuring head (Four Dimensions Inc.). The films were coated on Mylar, which is an insulating polymer, to prevent any current collector contribution during the measurement. The rest of the protocol was identical to the coating of conventional electrodes. The distance between the probes was about 1 mm each and the mass applied to the measuring head is 60 g. For reproducibility, the resistance was measured at 100 different locations on a 3x3 cm^2 coating square, and the test was repeated twice on 3 samples per formulation. Finally, the resistivity was determined according to Equation 7:

$$r = \frac{R \times S}{e} \text{ [}\Omega\text{.cm]} \quad (7)$$

With R (Ω) the measured resistance, S the contact area between the probe and the electrode coating, which is equal to 0.283 cm², and e (cm) the coating thickness.

Electrochemistry:

Electrodes were assembled in Swagelok cells in Ar filled glove box (O_2 and H_2O < 1 ppm) in half-cell configuration. The counter and reference electrode were metallic Li disc (diam. = 10 mm, thickness = 380 µm, 99.9%; Aldrich) placed on a Cu current collector (diam. = 12 mm, thickness = 250 µm). Two layers of glass microfiber membranes were used as separator (grade GF/D, diam. = 13 mm, thickness = 670 µm; Whatman). For some cells, an extra monolayer of polypropylene (PP) separator in contact with the Si electrode (grade 2500, diam. = 13 mm; Celgard) was used. As such, electrodes were protected from fiber inclusion coming from GF/D separators, which made easier their post-cycling observation by SEM. The separator layers were soaked with 300 µL of electrolyte made of 1 M $LiPF_6$ in ethylene carbonate (EC) and dimethyl carbonate (DMC) (1:1, v:v) plus 10 $_w$% of fluoroethylene carbonate (FEC) (99.9%; Solvionic). Si electrodes were cycled at room temperature using a multichannel VMP system (Biologic) in galvanostatic mode between 0.005 to 1 V (*vs.* Li^+/Li^0). The C rate was C/40 for the 1st cycle, C/20 for the next 5 cycles, and C/10 for the subsequent cycles (1C = 3820 $mA.g_{Si}^{-1}$ as Li_4Si was considered). Prior to cycling, cells were rested for 2 h at open circuit voltage (OCV). This period was set to 8 h for cells containing the extra PP layer in the separator (because of wetting issue with the electrolyte blend DMC). Cells were also relaxed at OCV for 10 s and 1 min after each discharge (lithiation) and charge step, respectively. For the sake of reproducibility, three to eight cells were tested for each Si electrode formulation, and the results were averaged.

Operando optical microscopy:

The morphological evolution of the electrode surface during cycling was observed *operando* using an ECC-Opto-Std-Aqu cell (El-cell). The electrodes were cycled following the same protocol as the Swagelok cells, except that a C/20 regime was applied. The potentiostat/galvanostat was an SP-300 (Biologic). The images were acquired with a DFC320 camera (LEICA) installed on a MEF4 M microscope (REICHERT). The cell had an observation window of 2 mm in diameter.

The electrode/separator stack was modified for the cell to work properly. In particular, some elements of the stack are holed to free the field of view up to the silicon electrode surface. In detail, from bottom to top, there was the quartz window, then an Li counter-electrode (diam. = 10 mm) with a hole in its center (diam. = 3.5 mm). Next, two layers of GF/D (diam. = 10 mm), also holed in the center (diam. = 2.5 mm), were used as separator. The hole in the separator

was smaller in order to hinder the Li dendrite propagation. Finally, the silicon electrode was set with a Cu spacer on its back (thickness = 250 µm), followed by a stainless-steel spring. The spring kept the stack compressed while the spacer protected the electrode which was too thin to support the spring pressure without any deformation.

During the first discharge, a gas bubble was generated by the SEI formation which blocked the field of view. Consequently, it was not possible to acquire sharp images over this period of time. To eliminate the bubble, the cycling was stopped after the first discharge (lithiation) and the cell electrolyte was renewed in the glove box. Only about 200 images could be opened simultaneously with the Image-Pro Plus 5.1 software due to the limited computer performance. To circumvent this issue, OCV steps were added to have enough time to save them and restart the acquisition. An in-house macro made with the Super Macro software was used to acquire images automatically every 5 to 10 minutes. The electrode surface was very regular such that it lacked in contrast at x20 magnification. As such, the CLAHE (local contrast enhancement) function (block size = 127, maximum slope = 2) of ImageJ was used to improve the contrast.

Supporting Information

Supporting Information is available from the Wiley Online Library or from the author.

Acknowledgements

Funding by the Natural Sciences and Engineering Research Council (NSERC) of Canada (grant RGPIN-2021-03374) is greatly acknowledged. Guillaume Berthout and Jiri Nohava from Anton Paar are gratefully acknowledged for the help with the nano-indentation experiments. Nicolas Stephant, Benoit Angleraud and Jonathan Hamon are gratefully acknowledged for the help with SEM, profilometry and XPS experiments, respectively.

Received: ((will be filled in by the editorial staff))
Revised: ((will be filled in by the editorial staff))
Published online: ((will be filled in by the editorial staff))

References

[1] J. Schwan, G. Nava, L. Mangolini, *Nanoscale Adv.* **2020**, *2*, 4368–4389.

[2] G.G. Eshetu, E. Figgemeier, *ChemSusChem.* **2019**, *12*, 2515–2539.

[3] D. Mazouzi, Z. Karkar, C. Reale Hernandez, P. Jimenez Manero, D. Guyomard, L. Roué, B. Lestriez, *J. Power Sources.* **2015**, *280*, 533–549.

[4] J.W. Hutchinson, Z. Suo, *Mixed Mode Cracking in Layered Materials*, Elsevier, **1991**.

[5] M.S. Hu, A.G. Evans, *Acta Metall.* **1989**, *37*, 917–925.

[6] F. Delannay, P. Warren, *Acta Metall. Mater.* **1991**, *39*, 1061–1072.

[7] Y. Xu, G. Yin, X. Cheng, P. Zuo, *Electrochimica Acta.* **2011**, *56*, 4403–4407.

[8] S. Lee, E.-S. Oh, *J. Power Sources.* **2013,** *244*, 721–725.

[9] H. Jeon, I. Cho, H. Jo, K. Kim, M.-H. Ryou, Y.M. Lee, *RSC Adv.* **2017**, *7*, 35681–35686.

[10] S. Basu, S. Suresh, K. Ghatak, S.F. Bartolucci, T. Gupta, P. Hundekar, R. Kumar, T.-M. Lu, D. Datta, Y. Shi, N. Koratkar, *ACS Appl. Mater. Interfaces.* **2018**, *10*, 13442–13451.

[11] D. Reyter, S. Rousselot, D. Mazouzi, M. Gauthier, P. Moreau, B. Lestriez, D. Guyomard, L. Roué, *J. Power Sources.* **2013**, *239*, 308–314.

[12] E. Ligneel, B. Lestriez, A. Hudhomme, D. Guyomard, *J. Electrochem. Soc.* **2007**, *154*, A235.

[13] E. Ligneel, B. Lestriez, O. Richard, D. Guyomard, *J. Phys. Chem. Solids.* **2006**, *67*, 1275–1280.

[14] P.R. Das, L. Komsiyska, O. Osters, G. Wittstock, *Synth. Met.* **2016**, *215*, 86–94.

[15] L. Huet, P. Moreau, N. Dupré, T. Devic, L. Roué, B. Lestriez, *Small Methods.* **2022**, *6*, 2200827.

[16] D. Mazouzi, R. Grissa, M. Paris, Z. Karkar, L. Huet, D. Guyomard, L. Roué, T. Devic, B. Lestriez, *Electrochimica Acta.* **2019**, *304*, 495–504.

[17] L. Huet, D. Mazouzi, P. Moreau, N. Dupré, M. Paris, S. Mittelette, D. Laurencin, T. Devic, L. Roué, B. Lestriez, Coordinatively crosslinked binders for silicon based electrodes for Li-ion batteries: beneficial impact on the mechanical properties and electrochemical performance, *Submitted*.

[18] C.R. Hernandez, A. Etiemble, T. Douillard, D. Mazouzi, Z. Karkar, E. Maire, D. Guyomard, B. Lestriez, L. Roué, *Adv. Energy Mater.* **2018**, *8*, 1701787.

[19] Y. Kishimoto, Y. Kobayashi, T. Ohtsuka, S. Ono, H. Yamazaki, Y. Tsukagoshi, K. Nakamura, *Mech. Eng. J.* **2020**, *7*, 19–00545.

[20] V. Vanpeene, P. Soucy, J. Xiong, N. Dupré, B. Lestriez, L. Roué, *J. Power Sources.* **2021**, *498*, 229904.

[21] Y. Oumellal, N. Delpuech, D. Mazouzi, N. Dupré, J. Gaubicher, P. Moreau, P. Soudan, B. Lestriez, D. Guyomard, *J. Mater. Chem.* **2011**, *21*, 6201.

[22] M.D. Thouless, *J. Vac. Sci. Technol. Vac. Surf. Films.* **1991**, *9*, 2510–2515.

[23] V. Vanpeene, J. Villanova, A. King, B. Lestriez, E. Maire, L. Roué, *Adv. Energy Mater.* **2019**, *9*, 1803947.

[24] S.C. Krishna, N.K. Gangwar, A.K. Jha, B. Pant, *J. Mater.* **2013**, *2013*, 1–6.

[25] R. Dhari, Vickers Hardness Number Calculator, https://www.omnicalculator.com/physics/vickers-hardness-number, accessed: July, **2022**.

[26] G. Liu, H. Zheng, X. Song, V.S. Battaglia, *J. Electrochem. Soc.* **2012**, *159*, A214–A221.

[27] D. Mazouzi, B. Lestriez, L. Roué, D. Guyomard, *Electrochem. Solid-State Lett.* **2009**, *12*, A215.

[28] J.-S. Bridel, T. Azaïs, M. Morcrette, J.-M. Tarascon, D. Larcher, *J. Electrochem. Soc.* **2011**, *158*, A750.

[29] F. Jeschull, F. Scott, S. Trabesinger, *J. Power Sources.* **2019**, *431*, 63–74.

[30] S. Jaiser, J. Kumberg, J. Klaver, J.L. Urai, W. Schabel, J. Schmatz, P. Scharfer, *J. Power Sources.* **2017**, *345*, 97–107.

[31] D. Guy, B. Lestriez, R. Bouchet, D. Guyomard, *J. Electrochem. Soc.* **2006**, *153*, A679.

[32] B. Lestriez, *Comptes Rendus Chim.* **2010**, *13*, 1341–1350.

[33] E. Panabière, J.-C. Badot, O. Dubrunfaut, A. Etiemble, B. Lestriez, *J. Phys. Chem. C.* **2017**, *121*, 8364–8377.

[34] K.W. Beard, *Linden's Handbook of Batteries, Fifth Edition*, McGraw-Hill Education, **2019**.

[35] A.N. Mistry, K. Smith, P.P. Mukherjee, *ACS Appl. Mater. Interfaces.* **2018**, *10*, 6317–6326.

[36] E. Pollak, G. Salitra, V. Baranchugov, D. Aurbach, *J. Phys. Chem. C.* **2007**, *111*, 11437–11444.

[37] Z. Karkar, D. Mazouzi, C.R. Hernandez, D. Guyomard, L. Roué, B. Lestriez, *Electrochimica Acta.* **2016**, *215*, 276–288.

[38] J. Xiong, N. Dupré, P. Moreau, B. Lestriez, *Adv. Energy Mater.* **2022**, 2103348.

[39] Z. Karkar, D. Guyomard, L. Roué, B. Lestriez, *Electrochimica Acta.* **2017**, *258*, 453–466.

[40] J. Xiong, N. Dupré, D. Mazouzi, D. Guyomard, L. Roué, B. Lestriez, *ACS Appl. Mater. Interfaces.* **2021**, *13*, 28304–28323.

[41] B. Lestriez, S. Bahri, I. Sandu, L. Roue, D. Guyomard, *Electrochem. Commun.* **2007**, *9*, 2801–2806.

[42] W.C. Oliver, G.M. Pharr, *J. Mater. Res.* **1992**, *7*, 1564–1583.

We investigate the copper current collector (CC) grade and ink solid fraction (SF) influence on silicon rich anodes, formulated with CMC/citric acid binder and possibly crosslinked by Zn(II) addition, through thorough inks and electrodes characterization. Electrochemical performance can be significantly improved for the former formulation, whereas the latter's performance shows little dependence on the CC and SF choice, but are always superior.

Lucas Huet, Hippolyte Houisse, Natalie Herkendaal, Thomas Devic, Lionel Roué, and Bernard Lestriez*

Impact of the Cu Current Collector Grade and Ink Solid Fraction on the Electrochemical Performance of Silicon-Based Electrodes for Li-Ion Batteries

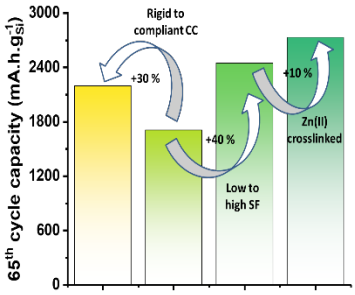

Supporting Information

Impact of the Cu Current Collector Grade and Ink Solid Fraction on the Electrochemical Performance of Silicon-Based Electrodes for Li-Ion Batteries

*Lucas Huet, Hippolyte Houisse, Natalie Herkendaal, Thomas Devic, Lionel Roué, and Bernard Lestriez**

Originally (historically, since 2009) the pH 3 buffer was prepared with KOH, but was subsequently replaced by NaOH to reduce the number of different cations in the binder solutions. This change eases chemical analysis and their interpretations and also reduces the "dead weight" in the electrode's compositions. We have verified here and in other works that the nature of the cation (K or Na) has no visible impact on the electrochemical performance. Each electrode composition is displayed Table S1.

Table S1. Comparison of electrodes' formulation depending on the cation used to make the pH 3 buffer

Formulation name		Electrode composition ($_w$%)					
Salt	*Coord. ratio*	*Silicon*	*Graphene*	*NaCMC*	*Citric acid*	*KOH or NaOH*	*Zn precursor*
Without Zn	0	73.4 73.6	11	7.2	7.4	1 0.8	0
$ZnSO_4$	0.22	69.9 70.1	10.5	6.8	7	1 0.7	4.8 4.9

Table S2. List of the electrodes and their mean 1st cycle electrochemical performance of every formulation cycled in Swagelok cells.

Formulations			Electrode dimensions		1st cycle electrochemical performance			
Salt	*Coord. Ratio*	*Solid fraction ($_w$%)*	*Current collector*	*Pores ($_v$%)*	*Discharge capacity (mAh.g_{Si}^{-1})*	*Charge capacity (mAh.g_{Si}^{-1})*	*CE (%)*	*Nbr. of electrodes*
Without Zn	0	21.4	Cold rolled	61 ± 0.3	4160 ± 30	3400 ± 80	81.1 ± 1.7	4
Without Zn	0	21.4	Annealed	60 ± 4	4000 ± 270	3360 ± 240	82.8 ± 6.4	6
Without Zn	0	21.4	Textured	63 ± 0.6	4090 ± 40	3470 ± 40	84.9 ± 0.5	3
Without Zn	0	27	Cold rolled	64 ± 1	4070 ± 90	3540 ± 40	87.0 ± 0.5	8
Without Zn	0	27	Annealed	73 ± 1	3830 ± 130	3300 ± 140	85.7 ± 2.4	7
Without Zn	0	27	Textured	63 ± 2	3900 ± 60	3390 ± 60	86.9 ± 0.6	3
$ZnSO_4$	0.22	22.3	Cold rolled	61 ± 2	4090 ± 160	3350 ± 170	84 ± 2	3
$ZnSO_4$	0.22	22.3	Annealed	63 ± 7	4170 ± 230	3590 ± 190	86.2 ± 0.4	4
$ZnSO_4$	0.22	22.3	Textured	62 ± 3	3690 ± 110	3160 ± 100	85.5 ± 0.5	3
$ZnSO_4$	0.22	28	Cold rolled	63 ± 1	4010 ± 160	3490 ± 170	86.9 ± 0.7	4
$ZnSO_4$	0.22	28	Annealed	59 ± 11	4100 ± 40	3620 ± 300	85.0 ± 1.1	4
$ZnSO_4$	0.22	28	Textured	59 ± 0.6	3690 ± 70	3140 ± 60	85.3 ± 0.3	3
W/o Zn+LiOH	0	21.5	Cold rolled	65 ± 0.7	4280 ± 130	3460 ± 90	81.8 ± 1.8	4
W/o Zn+LiOH	0	25.8	Cold rolled	65 ± 2	3940 ± 130	3610 ± 60	87.9 ± 0.9	4
ZnO	0.22	21.8	Cold rolled	62 ± 0.8	4140 ± 70	3610 ± 60	87.3 ± 0.5	3
ZnO	0.22	27.5	Cold rolled	66 ± 3	3950 ± 80	3390 ± 90	85.8 ± 1.5	8

Video S1 shows the morphological evolution during cycling of the surface of the Zn-free electrode (21.4% SF) with a C.-R. Cu CC, as observed by *operando* optical microscopy. Unfortunately, the particle contrast is very poor even at a magnification of 20x. At lower magnification of 10x (not shown), even the large cracks were barely visible. The first signs of

crack appearance happen around 250 mV during the delithiation. The electrode shrinkage is also visible on the coating island formed in the middle of the observed area. The left corner blurriness may come from the Li dendrite growth from the counter electrode. The hole in counter electrode creates an edge where the current density is higher. Therefore, during charge, dendrite growth occurs preferentially at this spot and thus is visible with the microscope. This blurriness could also be due to gas bubbles resulting from SEI formation. The region of interest (ROI) was changed before the second cycle lithiation. Cracks are also clearly visible in this ROI, and they close gradually during lithiation due to the coating volume expansion until a tension of around 50 mV is reached when they are completely closed. At the very end of the lithiation, the surface shakes and then protrude out of focus. This has been previously observed and is due to the electrode delamination.[1] In fact, when the crack close and the islands merge, the electrode volume expansion induces extra stress. This concentrates at the coating/current collector interface at the islands edges and might induce delamination,[2] which happened for our reference formulation.

The surface morphological evolution of the $ZnSO_4$ electrode (22.3% SF) with a C.-R. Cu CC, also acquired during cycling by *operando* optical microscopy, is presented in Video S2. Unfortunately, the first delithiation images were lost after computer crash during acquisition. At the beginning of the second cycle lithiation, one can see a bright spot on the right-hand top corner. This is a lithium dendrite on the counter electrode which appears blurry since it is out of focus. The silicon electrode Li^+ consumption during lithiation causes the dendrite to disappear. The cracks close completely around 70 mV and no delamination occurs after that. Some particles are bright, which we believe to be the lithiated graphene platelets. At the end of the lithiation, these get even brighter, which could come from the fact that graphene turns gold during the last lithiation stage (LiC_6).[3] During the second delithiation, the first cracks appear at approximately 250 mV, similarly to the Zn-free formulation electrode. Then, cracks keep widening without sign of new cracks appearing. For the third cycle, the ROI was changed. Cracks opened and closed from the same positions at each cycle, and the overall electrode behavior remains the same.

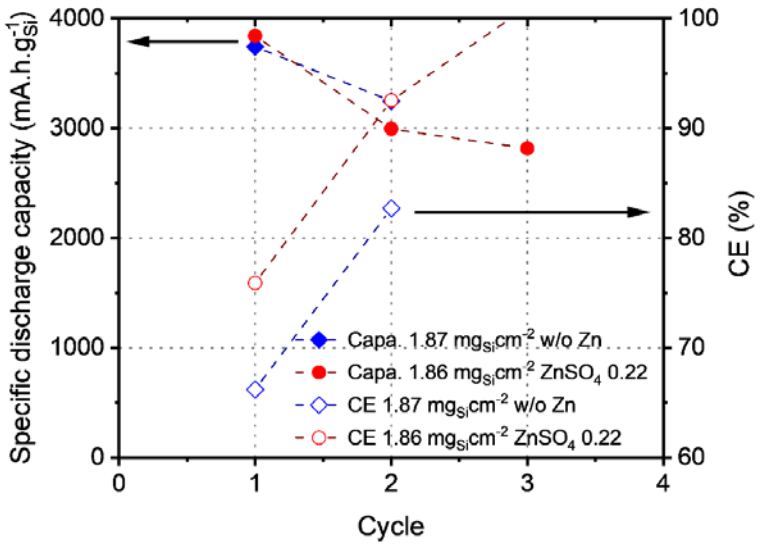

Figure S1. Electrochemical performance associated with Operando optical microscopy surface observations of electrodes with a C.-R. Cu CC: (Video S1) Zn-free formulation (21.4% SF) and (Video S2) $ZnSO_4$ formulation (22.3% SF).

Figure S1 shows the electrochemical performance of the *operando* optical microscopy tests for the Zn-free and $ZnSO_4$ electrodes observed in Videos S1 and S2, respectively. The specific discharge capacities and CE are lower than the ones obtained for electrodes cycled in Swagelok cells (by 14.9 and 8.6% points of CE, for the $ZnSO_4$ and its reference electrodes, respectively). The optical microscopy cell configuration degrades the electrode and separator stack (holed counter electrode and separator), which is probably the root of the inferior performances. Nonetheless, the electrodes deliver full discharge capacity for both formulations, though the charge capacities are much lower, as shown by the CE. Cracking formations shown in the Videos S1 and S2 represent those of highest stress/strain during lithiation and reduced stress/strain during delithiation. Finally, delamination is only observed in the case of the Zn-free electrode. Unfortunately, we cannot see if the rupture happens at the coating-Cu CC interface or in the coating bulk and therefore determine which fracture toughness is concerned.

Beuth Jr J. L.[4] *studied two types of cracks, one of which reaches the substrate interface, and the other propagates towards it but never reaches it. For the latter, which prevails in the case of compliant film on stiff substrate, the crack driving force becomes lower than the coating fracture resistance as the crack progress towards the interface. The in-depth crack observations on $ZnSO_4$ (22.3% SF) and its reference (21.4% SF) electrodes on an Ann. Cu CC Figure S2a and*

S2b, respectively, seems to agree with this result. This phenomenon was also observed with C.-R. and Txt. Cu CCs, but not shown here.

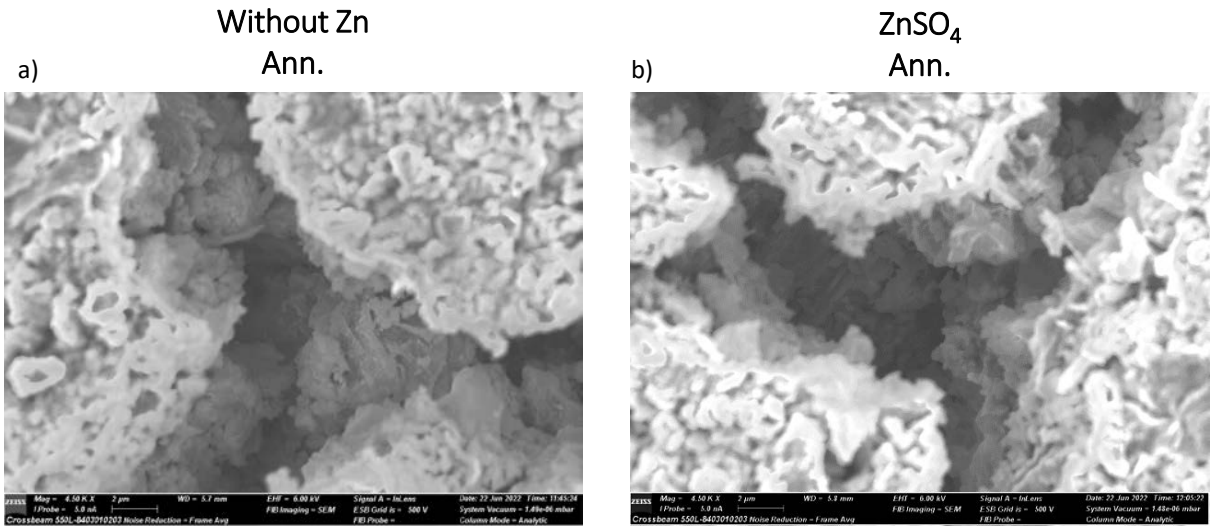

Figure S2. SEM observations inside surface cracks of electrodes with an Ann. Cu CC, after 1 cycle: (a) Zn-free formulation (21.4% SF); (b) $ZnSO_4$ formulation (22.3% SF).

Figure S3 shows SEM images of the different Cu CCs surface over a distance of around 20 µm and their respective roughnesses over a distance of 400 µm. For interpretation of those results, the reader is referred to the discussion accompanying Table 3 in the main text. Quantitative values of roughness were obtained from Figure S3b, S3d and S3f for the different Cu CCs and are available Table 3.

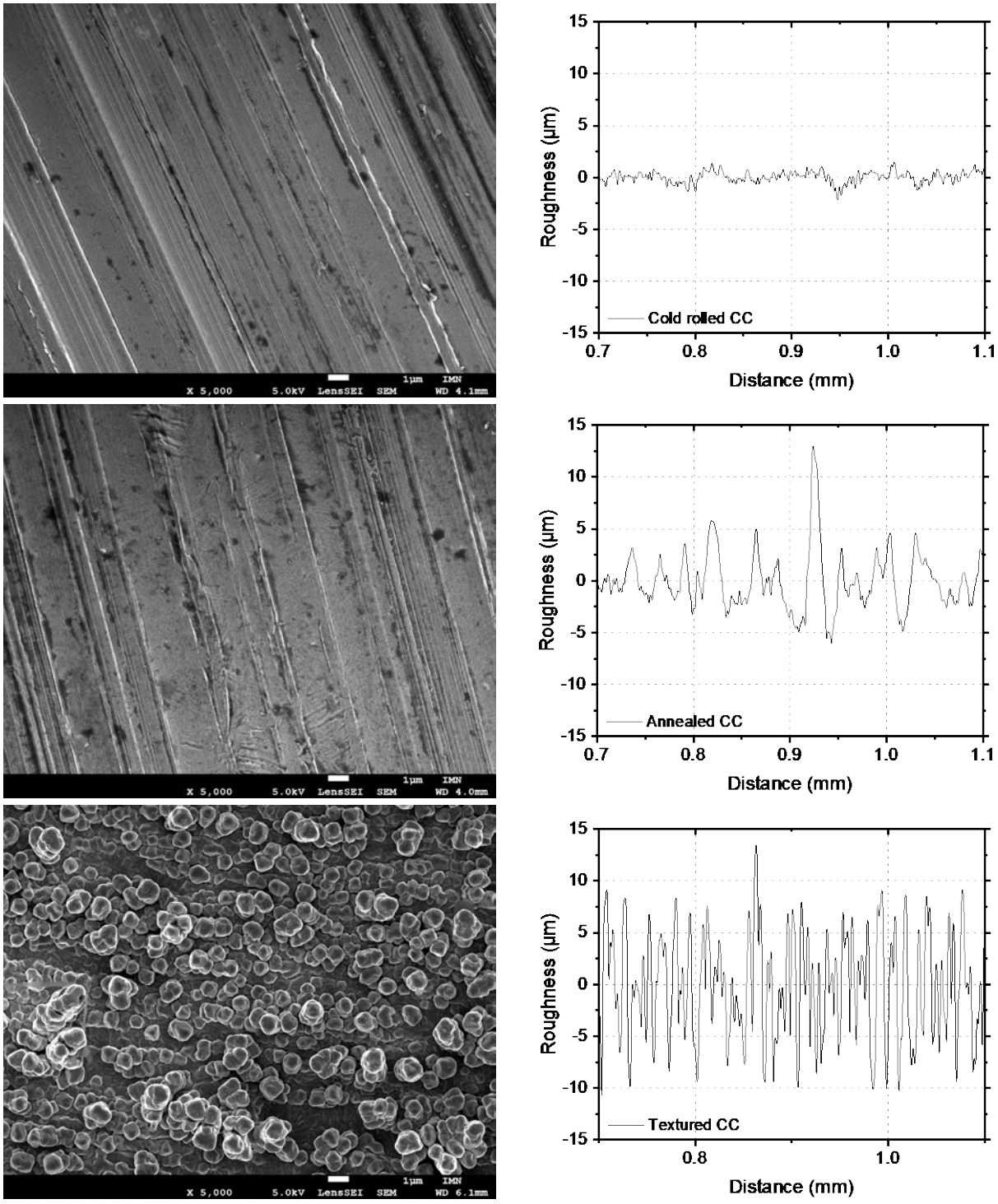

Figure S3. Cu CCs' surface SEM observations and roughness: (a, b) Cold rolled Cu CC; (c, d) Annealed Cu CC; (e, f) Textured Cu CC.

Figure S4 shows the XPS spectra with an analysis depth estimated to 10 nm of the 3 different Cu CCs focused, on the Cu 2p and Cu $L_3M_{4,5}M_{4,5}$ regions. The different peak positions were obtained graphically and are presented Table S2. No fitting was performed as only qualitative information on the surface composition was needed, and also because some Cu CC suffered

surface composition evolution under the beam. Indeed, the C.-R. and Ann. Cu CC surfaces present evolution over time that can be seen from the increasing intensity of the Cu $2p_{3/2}$ peak at 932.09 and 933.23 eV and Cu $2p_{1/2}$ peak at 951.98 and 952.97 eV, respectively (Figure S4a and S4c), with the red curves being the sum of the 5 first spectra and the blue ones being the sum of the 9 lasts spectra. For the C.-R. and Ann. CCs Cu LMM regions (Figure S4b and S4d, respectively), only the sum of the 5 first spectra is presented. For those samples, the Cu 2p and Cu LMM peaks position (Table S2)[5] and the samples evolution[6] correlates well with the presence of $Cu(OH)_2$ (presence of Cu 2p shake up structure peaks typical of Cu(II) species) and Cu_2O. However, for the Ann. Cu CC, the $Cu(OH)_2$ layer is much thicker as the Cu_2O Cu $2p_{3/2}$ and Cu $2p_{1/2}$ peaks are almost undiscernible. The Txt. Cu CC surface composition is different from the other two Cu CCs and did not evolved during the spectra acquisition. First, there is the presence of Cr(III) $2p_{3/2}$ and $2p_{1/2}$ peaks at respectively 576.21 and 586.14 eV in Figure S4f, which could be the signature of either $CuCr_2O_4$[7–9] or $CuCrO_2$[10–12] (the presence of Cr was also verified by EDX but is not shown). There is also the presence of two discernible Cu LMM peaks at around 916.85 and 918.5 eV (kinetic energy), which can be attributed to Cu_2O[5] and $CuCr_2O_4$,[9] respectively. The position of the two Cu $2p_{3/2}$ peaks Figure S4e at 932.49 and 934.36 eV also correlates very well with Cu_2O[5] and $CuCr_2O_4$,[7–9] respectively. For the latter the copper is in a +2 oxidation state which again matches perfectly with the presence of shake up structure peaks in the Cu 2p region.

X-ray diffraction measurement with a grazing incidence (1θ = 1 °, 15 to 60 2θ and 15 h of acquisition) was also performed on the Txt. Cu CC (not shown), no diffraction peaks except those of copper were present, such that no more information on the Cu CCs surface composition was obtained.

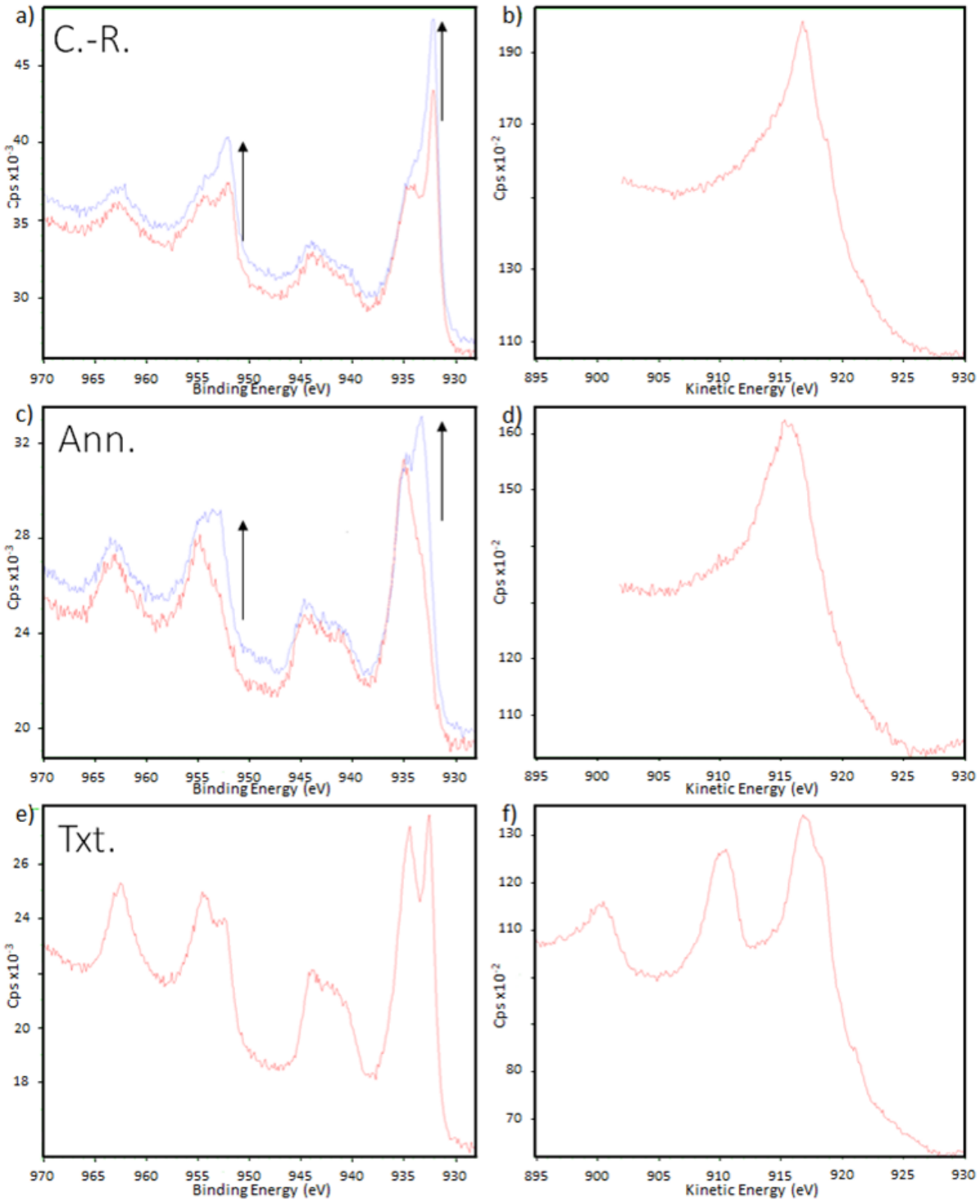

Figure S4. Cu CCs' XPS spectra focused on the Cu 2p and Cu LMM regions: (a, b) Cold rolled Cu CC, in red the sum of the 5 first spectra, in blue sum of the 9 next spectra; (c, d) Annealed Cu CC, in red the sum of the 5 first spectra, in blue sum of the 9 next spectra; (e, f) Textured Cu CC.

Peaks positions obtained graphically from Figure S4 are presented Table S3. For the Cu LMM peaks the position is expressed in terms of kinetic energy. For peaks attribution details, see Figure S4.

Table S3. XPS peaks position and their respective attribution to chemical species.

	Cu $2p_{3/2}$	Shake up peaks	Cu $2p_{1/2}$	Shake up structure peaks	Cr $2p_{3/2}$	Cr $2p_{1/2}$	Cu $L_3M_{4,5}M_{4,5}$	Peak attribution
Cold rolled Cu CC	932.09 934.3	944.01	951.98 954.18	962.62	/	/	916.78	Cu_2O $Cu(OH)_2$
Annealed Cu CC	933.23 934.95	944.59	952.97 954.77	963.03	/	/	915.63	Cu_2O $Cu(OH)_2$
Textured Cu CC	932.49 934.36	943.83	952.37 954.33	962.4	576.21	586.14	916.85 918.35	Cu_2O $CuCr_2O_4$

Table S4 summarizes the ZnO and respective reference formulations which are used in this study, and the corresponding electrode compositions. The $ZnSO_4$ being replaced with ZnO is particularly interesting because it significantly reduces the dead weight in the electrode composition, which is otherwise brought on by the sulfates. It also raises the binder pH solution up to 4.3 (compared to approximately 3.4 and 2.9 for the Zn-free and $ZnSO_4$ formulations, respectively). Therefore, LiOH was used in its reference binder formulation to similarly raise the pH (at around 4.4).

Table S4. ZnO and its reference formulations and their corresponding electrodes composition.

Formulation name	Electrode composition ($_w$%)						
Salt	*Coord. ratio*	*Silicon*	*Graphene*	*NaCMC*	*Citric acid*	*NaOH (+LiOH)*	*Zn precursor*
Zn-free + LiOH	0	73.1	11	7.2	7.3	0.7 +0.7	0
ZnO	0.22	71.8	10.8	7	7.2	0.7	2.5

Inks viscosity as a function of the shear rate for the Zn-free and $ZnSO_4$ formulation at different SF are illustrated in Figure S5a. The inks exhibit a shear-thinning behavior, which means that the viscosity decreases with increasing shear rate. The increased solid fraction significantly enhances the ink viscosity, mostly because the solvent volume is reduced such that particles interactions are favored. Note that for example, both 21.5% SF Zn-free + LiOH and 22.3% SF ZnO inks have the same volume of binder solution (*i.e.* 0.8 mL) and that both 27.1% SF Zn-free + LiOH and 27.5% SF ZnO inks have the same volume of binder solution (*i.e.* 0.59 mL) There are significant viscosity differences between the ZnO and respective reference inks for equivalent SF at 0.01 s^{-1}, which was not the case between $ZnSO_4$ and its reference inks (see Figure 4). Interestingly, the difference is reduced at the tape casting shear rate, of either 37 or 56 s^{-1} (*i.e.* h = 150 or 100 µm, with a casting speed of 5.6 $mm.s^{-1}$). The ink structure is destroyed by the shear rate and the polymer chains align with flow, such that most of the formulation's effect on the ink is likely reduced. Figure S5b and S5c summarize the viscosities and yield stresses, respectively, which were obtained around 0.01 s^{-1}, for every ink formulation at the different SFs. For descriptions, the reader is referred to the discussion accompanying Figure 4 and Table 4 in the main text.

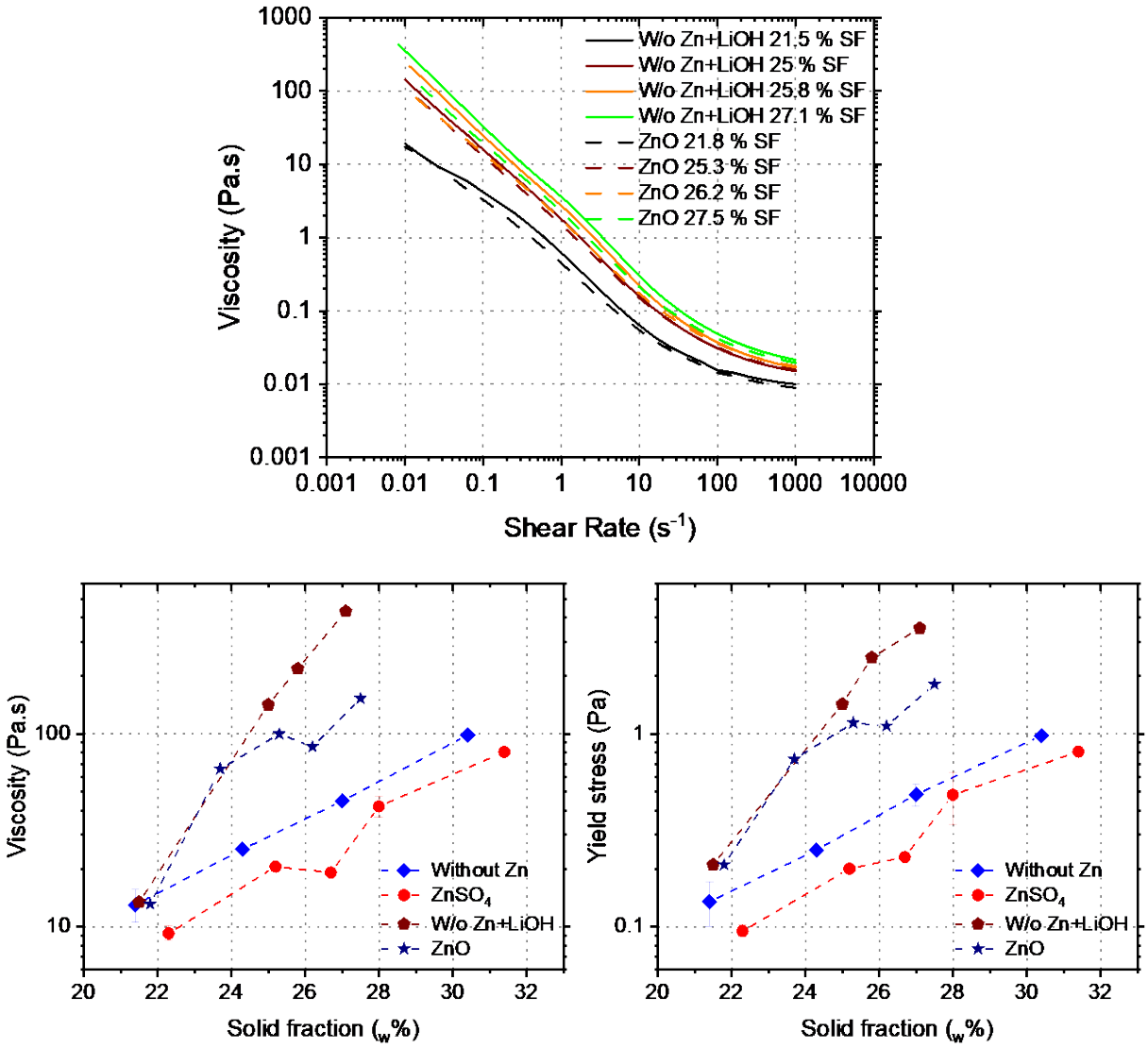

Figure S5. (a) Viscosity as a function of shear rate for Zn-free + LiOH and ZnO inks at different SF; (b) Summary of the viscosity obtained at a shear rate of approximately 0.01 s^{-1} as a function of the SF, for every formulation; (c) Summary of the yield stress calculated at a shear rate of approximately 0.01 s^{-1} as a function of the SF for each formulation.

Figure S6 present the specific discharge capacity and CEs of the formulations with ZnO at 21.8 and 27.5% SF and Zn-free with LiOH at 21.5 and 25.8% SF on a C.-R. Cu CC. When a higher SF is used, both the capacity retention and CE are enhanced for the Zn-free + LiOH formulation, though not for the ZnO electrodes. Namely, for the Zn-free formulation, the 60th cycle capacity is approximately 2180 *vs.* 1930 mAh.g_{Si}^{-1} and the 1st cycle CE is 87.9 *vs.* 81.2 for the 25.8 and 21.5% SF, respectively. For the ZnO formulation, the 60th cycle capacity is approximately 2310 *vs.* 2530 mAh.g_{Si}^{-1}, the 1st cycle CE is 85.8 *vs.* 87.1, and it stabilizes at around 99.3 *vs.* 99.3 from the 20th to the 65th cycle, for the 27.5 and 21.8% SF, respectively (though within std. dev. range for every parameter). Increasing the SF appears only beneficial for the Zn-free + LiOH electrodes

in this case. Nevertheless, whatever the SF is, the cyclability of the ZnO-based formulation remains superior to its reference formulation.

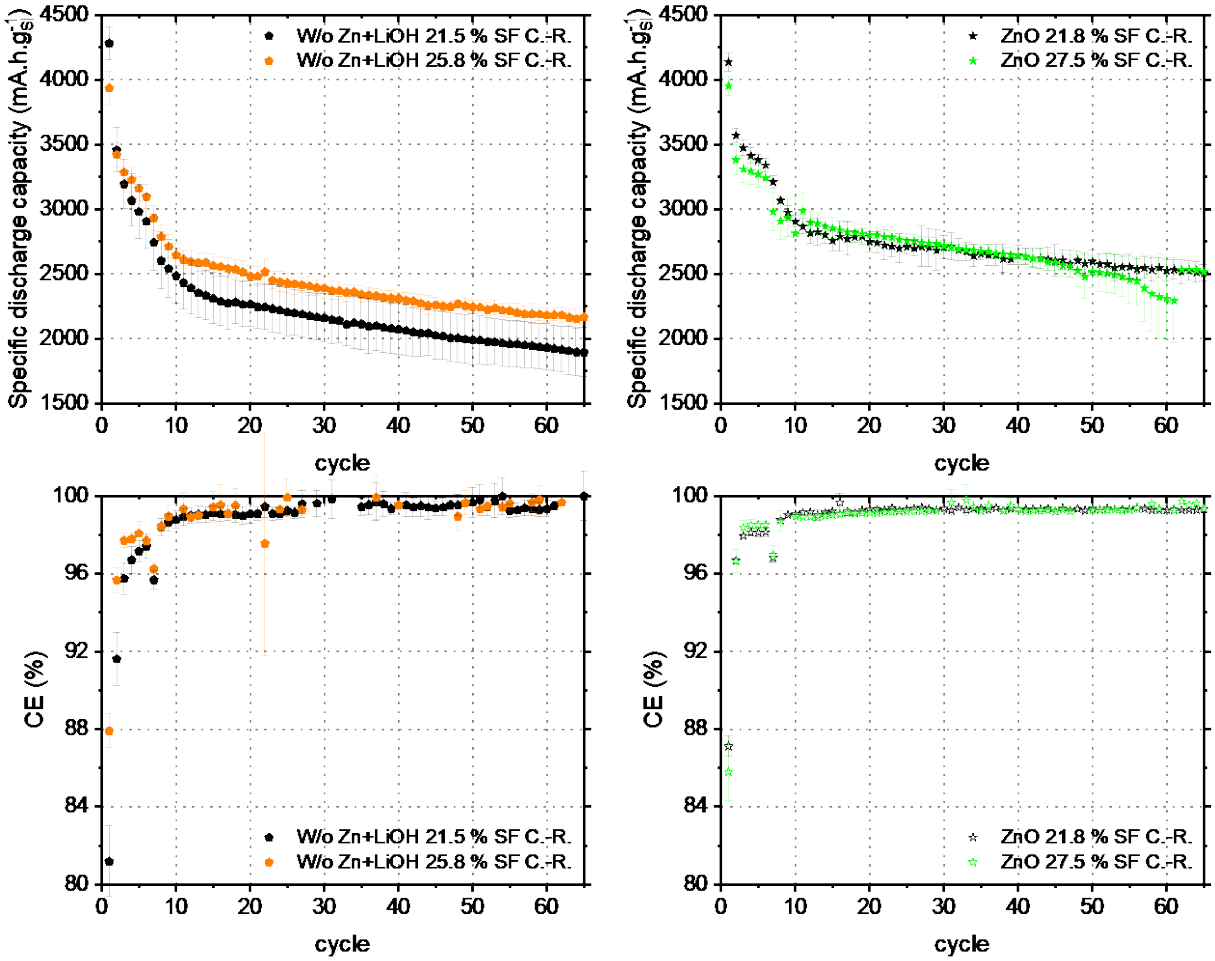

Figure S6. Specific discharge capacity and CE by cycle of electrodes prepared with different ink SFs and with a C.-R. Cu CC: (a, c) Zn-free + LiOH formulation; (b, d) ZnO formulation. The electrodes were cycled at C/40 for the 1st cycle, then C/20 for 5 cycles, and C/10 for the remaining cycles. The mean values and their standard deviation were determined from a minimum of 3 electrodes for each electrode formulation.

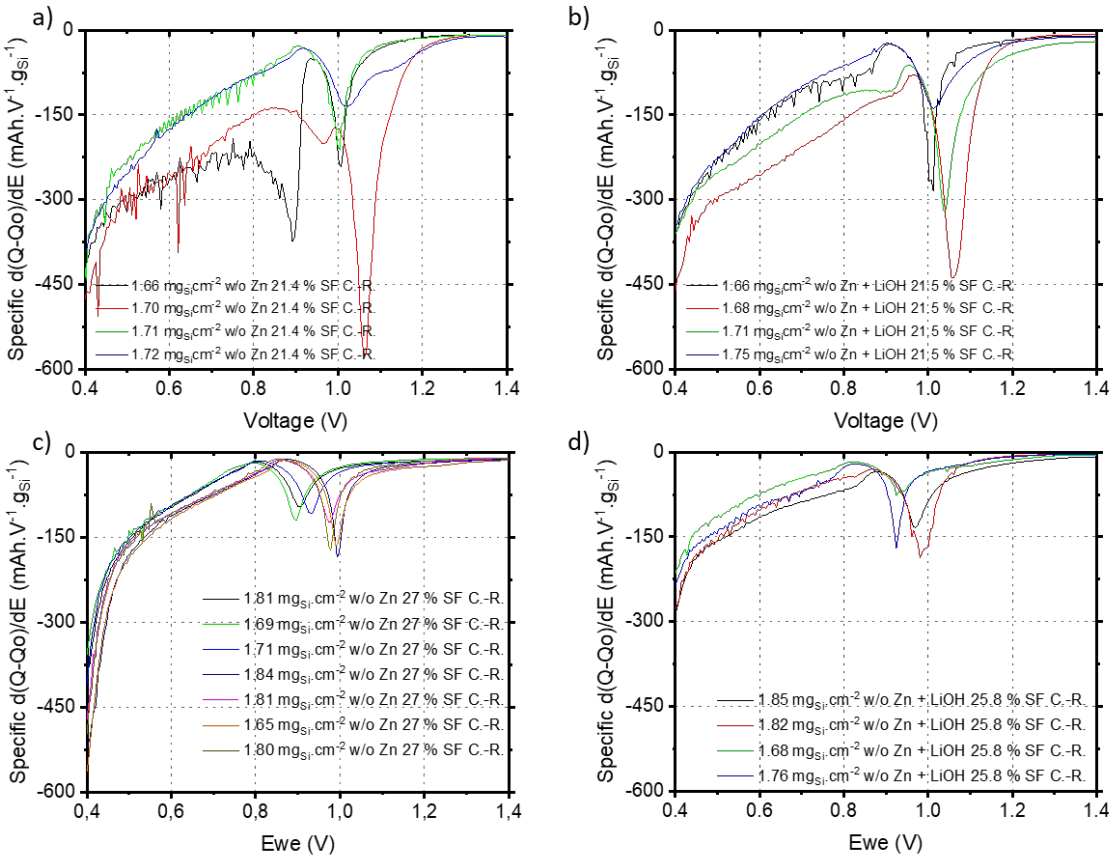

Figure S7. Incremental capacity curves at the first discharge in the 0.4-1.4 V potential window for a) Zn-free formulation prepared at the SF of 21.4%, b) Zn-free + LiOH formulation prepared at the SF of 21.5%, c) Zn-free formulation prepared at the SF of 27%, d) Zn-free + LiOH formulation prepared at the SF of 25.8%, all on C.R. Cu CCs.

Figure S8 present the specific discharge capacity and CE of the Zn-free formulation at 21.4 and 27% SF and the $ZnSO_4$ formulation at 22.3 and 28% SF, both coated on an Ann. Cu CCs. For both formulations, no clear SF impact was observed as the capacity retention and CE are very similar or within std. dev. range. Namely, for the Zn-free formulation, the 60th cycle capacity is approximately 2300 *vs.* 2230 mAh.g_{Si}^{-1} and the 1st cycle CE is 85.7 *vs.* 82.8%, for the 27 and 21.4% SF, respectively. For the $ZnSO_4$ formulation, the 60th cycle capacity is approximately 2680 *vs.* 2550 mAh.g_{Si}^{-1} and the 1st cycle CE is 85 *vs.* 86.2%, for the 28 and 22.3% SF, respectively.

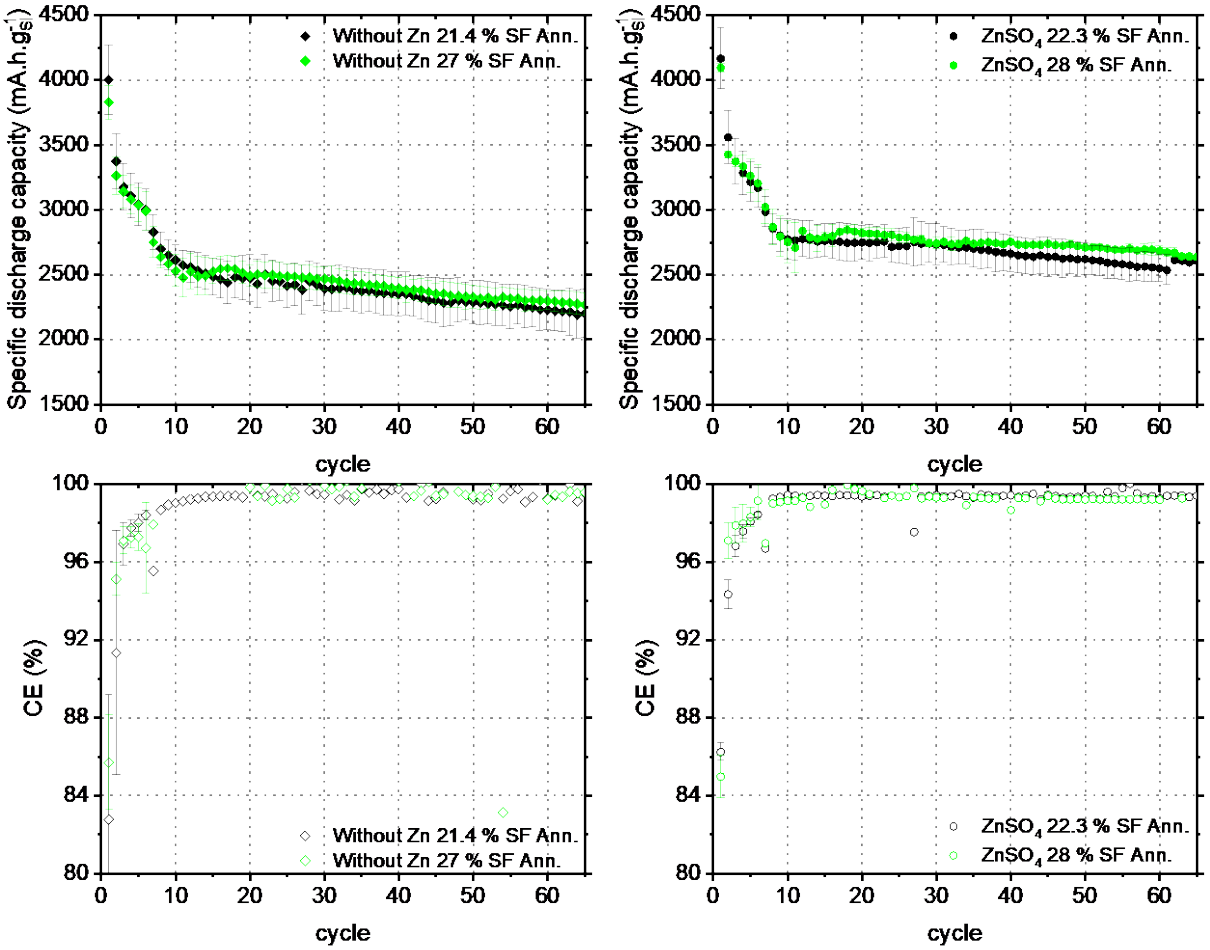

Figure S8. Specific discharge capacity and CE by cycle of electrodes prepared with different ink SFs and with an Ann. Cu CC: (a, c) Zn-free formulation; (b, d) ZnSO4 formulation. The electrodes were cycled at C/40 for the 1st cycle, then C/20 for 5 cycles, and C/10 for the remaining cycles. The mean values and their standard deviation were determined from a minimum of 3 electrodes for each electrode formulation.

Figure S8 present the specific discharge capacity and CE of the Zn-free formulation at 21.4 and 27% SF and the $ZnSO_4$ formulation at 22.3 and 28% SF, both coated on Txt. Cu CCs. For both formulations, a slight improvement was observed in the capacity retention with increasing SF. Namely, for the Zn-free formulation, the 60th cycle capacity is approximately 2150 *vs.* 1930 mAh.g_{Si}^{-1} and the 1st cycle CE is 86.9 *vs.* 84.9%, for the 27 and 21.4% SF, respectively. For the $ZnSO_4$ formulation, the 60th cycle capacity is approximately 2460 *vs.* 2320 mAh.g_{Si}^{-1} and the 1st cycle CE is 85.3 *vs.* 85.5%, for the 28 and 22.3% SF, respectively.

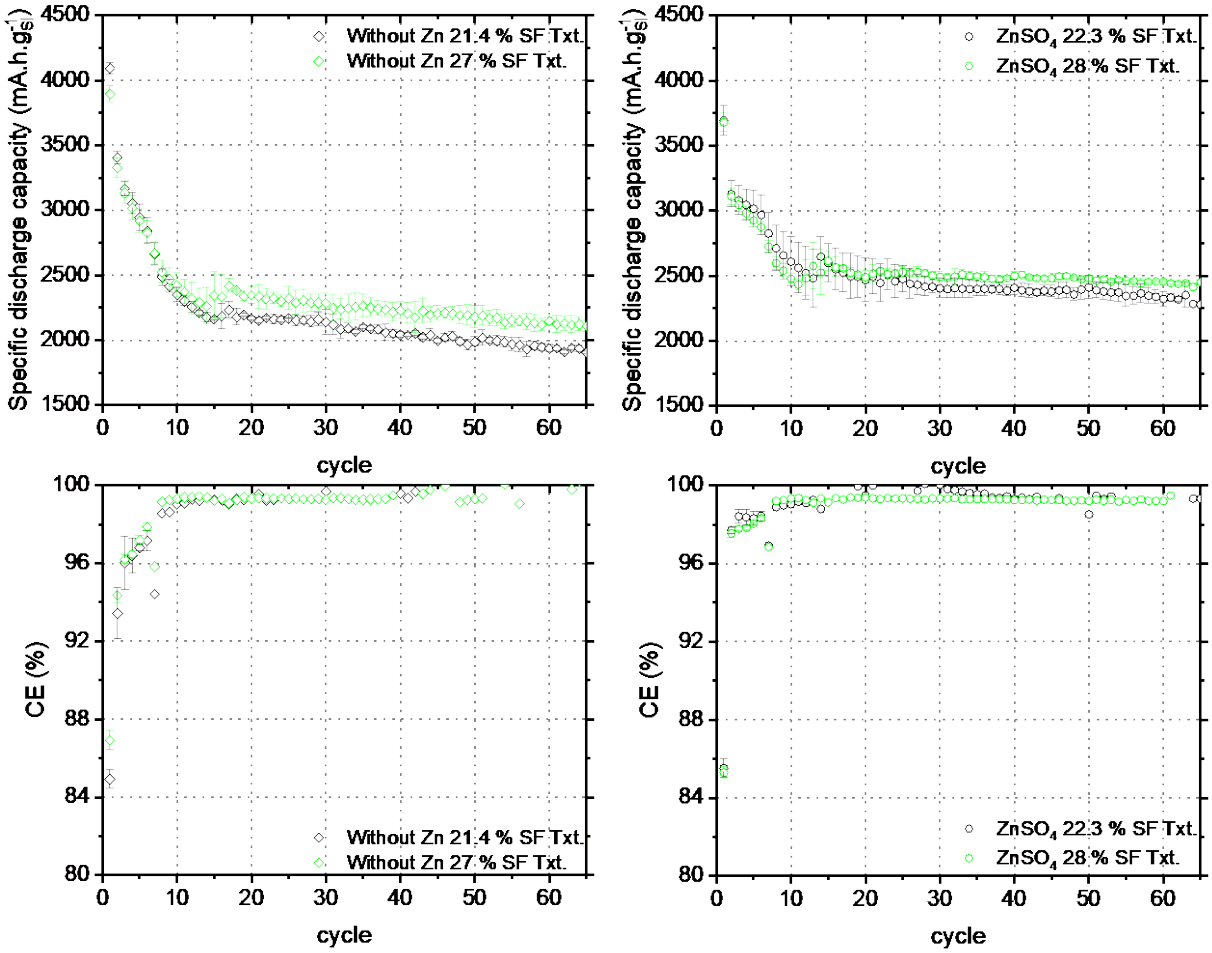

Figure S9. Specific discharge capacity and CE by cycle of electrodes prepared with different ink SFs and with a Txt. Cu CC: (a, c) Zn-free formulation; (b, d) $ZnSO_4$ formulation. The electrodes were cycled at C/40 for the 1st cycle, then C/20 for 5 cycles, and C/10 fir the remaining cycles. The mean values and their standard deviation were determined from a minimum of 3 electrodes for each electrode formulation.

References

[1] C.R. Hernandez, A. Etiemble, T. Douillard, D. Mazouzi, Z. Karkar, E. Maire, D. Guyomard, B. Lestriez, L. Roué, A Facile and Very Effective Method to Enhance the Mechanical Strength and the Cyclability of Si-Based Electrodes for Li-Ion Batteries, Adv. Energy Mater. 8 (2018) 1701787. https://doi.org/10.1002/aenm.201701787.

[2] V. Vanpeene, J. Villanova, A. King, B. Lestriez, E. Maire, L. Roué, Dynamics of the Morphological Degradation of Si ‐ Based Anodes for Li ‐ Ion Batteries Characterized by In Situ Synchrotron X ‐ Ray Tomography, Adv. Energy Mater. 9 (2019) 1803947. https://doi.org/10.1002/aenm.201803947.

[3] G. Zeng, R. Zhang, Y. Tan, X. Cheng, T. Jiang, Graphene-Based Tunable Coloration Film through Intercalation, ACS Photonics. 8 (2021) 3599–3606. https://doi.org/10.1021/acsphotonics.1c01223.

[4] J.L. Beuth, Cracking of thin bonded films in residual tension, Int. J. Solids Struct. 29 (1992) 1657–1675. https://doi.org/10.1016/0020-7683(92)90015-L.

[5] M.C. Biesinger, Advanced analysis of copper X-ray photoelectron spectra: Advanced analysis of copper X-ray photoelectron spectra, Surf. Interface Anal. 49 (2017) 1325–1334. https://doi.org/10.1002/sia.6239.

[6] X-ray Photoelectron Spectroscopy (XPS) Reference Pages, (n.d.). http://www.xpsfitting.com/search/label/Copper (accessed November 29, 2022).

[7] W. Yuan, X. Liu, L. Li, Synthesis, characterization and photocatalytic activity of cubic-like CuCr2O4 for dye degradation under visible light irradiation, Appl. Surf. Sci. 319 (2014) 350–357. https://doi.org/10.1016/j.apsusc.2014.07.158.

[8] S.S. Acharyya, S. Ghosh, S. Adak, T. Sasaki, R. Bal, Facile synthesis of $CuCr_2O_4$ spinel nanoparticles: a recyclable heterogeneous catalyst for the one pot hydroxylation of benzene, Catal Sci Technol. 4 (2014) 4232–4241. https://doi.org/10.1039/C4CY00615A.

[9] Joen.J. Hermans, L. Baij, M. Koenis, K. Keune, P.D. Iedema, S. Woutersen, 2D-IR spectroscopy for oil paint conservation: Elucidating the water-sensitive structure of zinc carboxylate clusters in ionomers, Sci. Adv. 5 (2019) eaaw3592. https://doi.org/10.1126/sciadv.aaw3592.

[10] D. Xiong, H. Chang, Q. Zhang, S. Tian, B. Liu, X. Zhao, Preparation and characterization of CuCrO2/TiO2 heterostructure photocatalyst with enhanced photocatalytic activity, Appl. Surf. Sci. 347 (2015) 747–754. https://doi.org/10.1016/j.apsusc.2015.04.188.

[11] G.C. Allen, M.T. Curtis, A.J. Hooper, P.M. Tucker, X-Ray photoelectron spectroscopy of chromium–oxygen systems, J Chem Soc Dalton Trans. (1973) 1675–1683. https://doi.org/10.1039/DT9730001675.

[12] G.C. Allen, P.M. Tucker, Multiplet splitting of X-ray photoelectron lines of chromium complexes. The effect of covalency on the 2p core level spin-orbit separation, Inorganica Chim. Acta. 16 (1976) 41–45. https://doi.org/10.1016/S0020-1693(00)91689-X.